

# Speedup of self-propelled helical swimmers in a long cylindrical pipe

Ji Zhang(张骥)<sup>1</sup>, Kai Liu(刘凯)<sup>1</sup>, and Yang Ding(丁阳)<sup>1,2,†</sup>

<sup>1</sup>Beijing Computational Science Research Center, Beijing 100193, China

<sup>2</sup>Beijing Normal University, Beijing 100875, China

(Received 13 September 2021; revised manuscript received 14 October 2021; accepted manuscript online 27 October 2021)

Pipe-like confinements are ubiquitously encountered by microswimmers. Here we systematically study the ratio of the speeds of a force- and torque-free microswimmer swimming in the center of a cylindrical pipe to its speed in an unbounded fluid (speed ratio). Inspired by *E. coli*, the model swimmer consists of a cylindrical head and a double-helical tail connected to the head by a rotating virtual motor. The numerical simulation shows that depending on swimmer geometry, confinements can enhance or hinder the swimming speed, which is verified by Reynolds number matched experiments. We further developed a reduced model. The model shows that the swimmer with a moderately long, slender head and a moderately long tail experiences the greatest speed enhancement, whereas the theoretical speed ratio has no upper limit. The properties of the virtual motor also affect the speed ratio, namely, the constant-frequency motor generates a greater speed ratio compared to the constant-torque motor.

**Keywords:** microswimmer, confinement, low Reynolds number, creeping flow

**PACS:** 47.15.G, 47.63.Gd, 87.17.Jj, 87.16.Qp

**DOI:** 10.1088/1674-1056/ac339a

## 1. Introduction

Microswimmers such as bacteria commonly swim in confined spaces such as soils and tissues. The effect of confinement on the mobility behavior of microswimmers has implications in biofilm formation,<sup>[1]</sup> micro manipulation,<sup>[2,3]</sup> and biomedical processes,<sup>[2,4]</sup> hence has attracted continuing research efforts.

Previous studies showed that boundaries and confinement can affect the swimming speed of microswimmers. For example, the forward speed of the sperm decreases monotonically in the pipes until the pipe diameter is small enough to forbid mobility of the sperm.<sup>[5]</sup> The speed of bimetallic microswimmers can increase up to 5 times due to the electrostatic and electrohydrodynamic boundary effects.<sup>[6]</sup> Several theoretical and numerical studies have shown enhancement of the swimming speed with confinements in various idealized systems, including dipolar microswimmer,<sup>[7]</sup> infinite waving sheet,<sup>[8]</sup> and spherical squirmers.<sup>[9,10]</sup>

As many microswimmers use helical flagella for propulsion (e.g., *E. coli*), the thrust and motion of simple helical structures in confinements have been studied extensively. Including a passive head, Caldag *et al.*<sup>[11]</sup> experimentally studied the motion of a magnetically driven helical microswimmer in a pipe. With a fixed geometry of the swimmer, they found that the swimming speed varied little in two cylinders with different radii. Felderhof<sup>[12]</sup> presented an analytical solution for a slender, infinite helix swimmer in the cylindrical pipe using the perturbation method and reported an enhancement of speed due to the confinement. Liu *et al.*<sup>[13]</sup> verified the speed enhancement phenomenon numerically using a boundary ele-

ment method. They calculated the swimming efficiency of the helical flagella, and found that the optimal geometry is similar to that of *E. coli* and does not depend on confinement.

While much is known for the thrust generation and the swimming of simple helical structures driving externally, the influence of the confinement to the speed of self-propelled microswimmers still needs to be clarified. An experimental study by Vizsnyiczai *et al.*<sup>[14]</sup> demonstrated that the forward speed of *E. coli* in a square tunnel with a width of about 2.3  $\mu\text{m}$  reaches a maximal speed 1.1 times the free speed. They attributed the speedup to the decrease of the wobbling amplitude due to the confinement. Acemoglu and Yesilyurt studied a self-propelled microswimmer in a finite pipe numerically.<sup>[15]</sup> The swimmer consists of a spheroid head and a single helical tail. They varied the geometric parameters of the pipe and swimmer and observed a maximum speed enhancement of  $\sim 30\%$  depending on the ratio of pipe to head radius. However, the assumption that the spin of the tail is a constant relative to the lab frame rather than to the body of the swimmer is unphysical.

Although the speed enhancement of helical swimmers in confinements is repeatedly observed in simulations and experiments, it is still unclear if the enhancement is possible on a self-propelled swimmer purely due to hydrodynamic effects. The dependence of the enhancement in the swimming speed on the geometric parameters of the helical swimmer and the confinement is also not well understood. Here, we develop a numerical model based on a simplified double-helix swimmer in an infinite pipe to study the variation of the speed ratio, and verified the phenomenon experimentally. We further develop

<sup>†</sup>Corresponding author. E-mail: dingyang@csrc.ac.cn

a reduced model to extend the ranges of parameters to discuss the optimal geometry that results in maximum speed enhancement, and explore the upper limit of the speed enhancement.

## 2. Models and validations

### 2.1. Model system

We consider an *E. coli*-like helical swimmer inside an infinitely long cylinder filled with Newtonian fluid. As shown in Fig. 1(a), the microswimmer consists of a rigid cylindrical head with round ends and a rigid double-helical tail. These two parts are connected by a virtual motor that the hydrodynamical effect is negligible. The microswimmer is placed along the pipe center-line. Geometrical parameters of the microswimmer are shown in Fig. 1(a), including the radius of the pipe  $R$ , the radius of the head  $r_h$ , the radius of the tail  $r_t$ , the lengths of the head  $l_h$  and the tail  $l_t = n\lambda$ , the pitch of the helical tail  $\lambda$ , the number of periods  $n$ , and the length of the virtual motor  $\delta_{ht}$ . We normalize the length of the model using the radius of tail  $r_t$ .

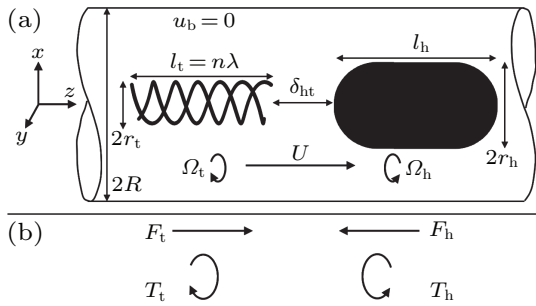


**Fig. 1.** (a) The diagram of the microswimmer in an infinitely long pipe. The microswimmer is placed along the axis of the pipe. The head and the tail rotate in opposite directions. Geometrical and kinetic parameters are illustrated in the figure. (b) Hydrodynamically reduced model of the microswimmer. The forces and torques on the head and tail from the fluid are  $(F_h, T_h)$  and  $(F_t, T_t)$ .

The virtual motor generates a spin  $\Omega_{sw}$  that rotates the head in the counterclockwise direction with an angular speed  $\Omega_h$ , and rotates the tail in the opposite direction with an angular speed  $\Omega_t = \Omega_h + \Omega_{sw}$ . The rotation of the helix generates a thrust and results in a forward velocity  $U(R)$  in the pipe with a radius  $R$ . Then  $U^\infty = U(\infty)$  is the velocity in the free space and the speed ratio is defined as

$$\alpha = \frac{U(R)}{U(\infty)}. \quad (1)$$

Due to the symmetry of the body geometry of the swimmer, the translational and rotational velocities of the swimmer have only non-zero components along the axis.

We assume that the fluid moves at the creeping flow regime so that the governing equations of the velocity  $\mathbf{u}$  are

$$\nabla \cdot \mathbf{u} = 0, \quad (2)$$

$$\mu \nabla^2 \mathbf{u} = \nabla p, \quad (3)$$

where  $p$  is the pressure, and  $\mu$  is the fluid viscosity. We apply the no-slip boundary conditions on the surface of the pipe

$$\mathbf{u}(\mathbf{x}_b) = 0, \quad (4)$$

and on the surface of the microswimmer

$$\mathbf{u}(\mathbf{x}_h) = (0, 0, U) + (0, 0, \Omega_h) \times \mathbf{r}_h, \quad (5)$$

$$\mathbf{u}(\mathbf{x}_t) = (0, 0, U) + (0, 0, \Omega_t) \times \mathbf{r}_t, \quad (6)$$

where  $\mathbf{r}_h$  and  $\mathbf{r}_t$  indicate the relative position of the surface of the microswimmer with respect to the center of the head, respectively. Since inertia is negligible for microswimmers, the self-propelling microswimmer satisfies the force- and torque-free conditions.

The output characteristics of the motor also influence the speed of the swimmer under different confinements, hence influence the speed ratio. Previous studies on several kinds of bacteria have shown that the motors in bacteria have similar output characteristics: at low spin speed the torque is nearly constant and at high spin speed the torque decreases.<sup>[16,17]</sup> Therefore, we mainly focus on the constant torque case, and without losing generality, we assume unit motor torque  $T_{sw} = 1$ . We will also consider the constant-frequency  $\Omega_{sw} = 1$  and the constant power  $P_{sw} = \Omega_{sw} T_{sw} = 1$  cases. Taking advantage of the linearity of the system, we only need to scale the speed from one of the cases to get the swimming speeds for the others.

### 2.2. Numerical solution

We first solve the motion of the swimmer and fluid flow explicitly using the method of Stokeslets.<sup>[18,19]</sup> We perform full three-dimensional simulations in this study and compute the swimming velocities in all 6 degrees of freedom. We find the lateral component of the swimming speed is less than 0.1% of the forward speed in all cases we tested, consistent with our previous analysis. The linearity of the Stokes equations allows us to decompose the flow fields in terms of fundamental singular solutions of point forces, namely, Stokeslets. By solving a matrix equation connecting the singularity forces and boundary velocities, the flow field and boundary forces can be obtained. Since the relations between the forces and velocities, and torques and angular velocities of the swimmer are also linear, the force- and torque-free equations for the head and tail can be added to the matrix equations for the fluid.<sup>[19-21]</sup> Then the swimming speed and the rotation of the head and tail can be obtained at the same time as the flow.

The method of Stokeslets has the ability to capture different boundary conditions by applying appropriate Stokeslets. The most commonly used one is the Stokeslets in three-dimensional infinite space

$$\mathbf{S}(\mathbf{x}, \mathbf{x}_f) = \frac{1}{8\pi\mu} \left( \frac{\mathbf{I}}{r} + \frac{(\mathbf{x} - \mathbf{x}_f)(\mathbf{x} - \mathbf{x}_f)}{r^3} \right), \quad (7)$$

which connects the velocity at a point in the space  $\boldsymbol{x}$  and a point force at  $\boldsymbol{x}_f$ . For the Stokeslets in a pipe with zero velocity on the pipe surface, Liron and Shahar have developed a series expression.<sup>[22]</sup> However, the series expression has a convergence problem when applied to a continuous surface such as the head of the swimmer. To describe the boundary velocity accurately on a continuous surface, the distance of the point force should be small. But the convergence rate of the series is exponentially slow near the point force, especially along the direction of the cylinder axis. We solve this problem by using the series expression for points with large distances from the point force and use free-space Stokeslets (Eq. (7)) with corrections from the confinement for nearby points. For the details of reconstructing the Stokeslets in pipe and the validation of the method, see Appendix A.

### 2.3. Physical model

To verify that a self-propelled swimmer can change speed because of only hydrodynamical effects and validate our numerical models, we developed a physical model — a robot (Fig. 2). The shells of the head and the tail are 3D printed using Resin V4 Tough 3D material (Huaxia Plastic Co.). The head radius is  $r_h = 11.2$  mm, and the head length is  $l_h = 123.40$  mm. Different from the simulation, a thin rod with radius  $\rho_{ht} = 2$  mm and length  $\delta_{ht} = 13$  mm is required to connect the motor and the tail. The flagella radius of the tail is  $\rho_t = 2.5$  mm.

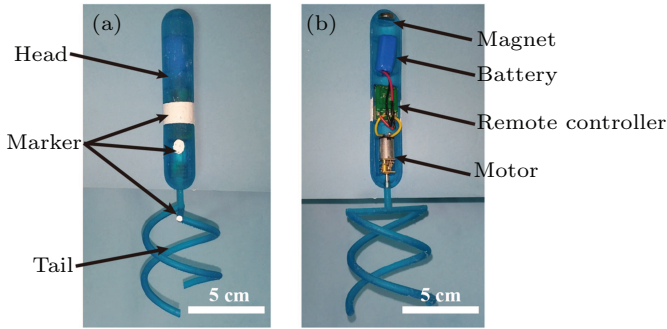


Fig. 2. The outside (a) and inside (b) views of the flagellated robot.

We reproduced the phenomena of speedup and slow down by changing the tail shape. Inside the robot head, a motor (model JGA-N20-298, ASLONG MOTOR Co., 40 RPM, 11 kg·mm), a remote-controlled infrared switch, and a lithium-ion battery (7.4 V, 350 mA·h, ZON.CELL Co.) are serially connected (see Fig. 2(b)). A white line and a white dot were drawn on the head of the robot, and a white dot was also drawn on the tail of the robot for video tracking. We adjust the weight of the swimmers by putting in metal chips, such that the robot has neutral buoyancy in the fluid. The neutral buoyancy is confirmed by examining the movement of the robot while power off. The speed of the robot in the fluid with the motor off is less than 1% of the speed when the motor is on.

To make the Reynolds number comparable to biological systems, we used silicone oil with a kinematic viscosity of  $10^5$  cSt. As the robot tail can spin at about 40 rad/min, the corresponding Reynolds number is less than  $10^{-2}$ . We further filled the gaps with silicone grease to prevent the liquid getting into the robot during the experiments. The total depth of the fluid is 500 mm, about four times the robot's length. We approximate the infinite volume of fluid by using a cylinder with a radius of 147 mm, more than ten times of the robot's head radius. To minimize the influence of the surface boundary of the fluid, the data was collected when the robot is 150 mm below the surface of the fluid and 150 mm above the bottom of the container. A magnet was used to adjust the orientation of the robot and align its axis with the axis of the cylindrical container before the experiment started. The robot can swim 70–100 mm per minute. The motion of the robot was recorded by a camera at a time interval of 300 ms. We calibrated the image with a scale in the fluid for small optical distortions. The trajectories of the robots were obtained by tracking the markers on the robots. Each case was repeated 3 times.

### 2.4. Comparison of speeds from experiments and numerical simulations

We compared the speed ratio of two typical kinds of microswimmers, one with a big tail and another one with a small tail. The geometrical parameters of the microswimmers are listed in Table 1.

Table 1. Geometric parameters of microswimmers in the simulation and the experiment.

	Experiment		Simulation	
	big tail	small tail	big tail	small tail
$r_h$	11.20 mm	11.20 mm	0.43	1.24
$l_h$	123.40 mm	123.40 mm	4.76	13.71
$n$	0.5	0.5	0.5	0.5
$\lambda$	62.00 mm	85.00 mm	2.39	9.44
$r_t$	25.90 mm	9.00 mm	1	1
$\rho_t$	2.5 mm	2.5 mm	0.097	0.27
$\delta_{ht}$	13 mm	13 mm	0.50	1.44
$\rho_{ht}$	2 mm	2 mm	0.077	0.22

We found that the speed ratio depends on the geometry of the swimmer, especially the ratio of the head size to the tail size. For the swimmer with a small tail, the speed decreases monotonously with the stronger confinement in Fig. 3(a). In contrast, the speed of the swimmer with a big tail increases at first and then decreases as the confinement becomes stronger, as shown in Fig. 3(b).

Although there is a system error between experimental and numerical results, the phenomenon is verified, and the speed ratio is close to the simulation results. We attribute the discrepancy to the minor differences in the configurations, such as the connecting rod and surface effects.

The numerical results showed that, for the big tail case, the speed ratio reaches the peak at  $r_t/R \approx 1/0.7$ , consistent with the previous study on a single helix.<sup>[13]</sup> Since the increase of propulsion is the greatest when  $r_t/R \approx 1/0.7$  for the tail, we use this value for the rest of the paper.

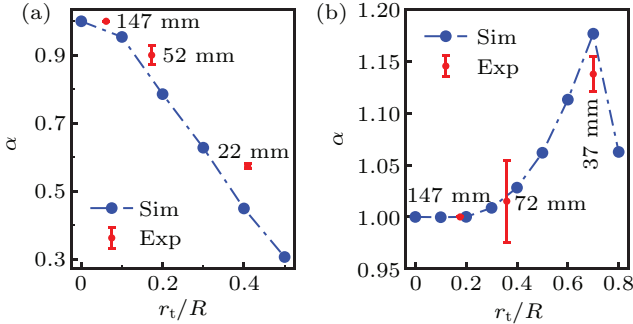


**Fig. 3.** The speed ratio  $\alpha$  of microswimmer as a function of the ratio between the radius of the tail and the radius of the pipe, defined as  $r_t/R$ . (a) The microswimmer with a small tail slows down in the pipe. (b) The microswimmer with a big tail speedup in the pipe. The blue dots show the simulation results, and the red dots with the error bar show the experimental results. The labels indicate the pipe radii in the experiments. All the speeds are normalized such that the spin of the motor is a constant 1.

More numerical test cases implied that the length of the tail plays an important role in determining the speed of the swimmer, but the long tails are computationally intensive for numerical simulation. Therefore, to better understand this speedup phenomenon, we developed a reduced model.

## 2.5. Reduced model

Take advantage of the symmetry, the head and tail can only translate and rotate along the axis of the pipe. Due to the constrain by the connecting rod,  $U_{\text{head}} = U_{\text{tail}} = U$ . We further neglect the hydrodynamical coupling between the head and tail and then the motions of the head and tail are related to the forces and torques on them by the following linear equations:<sup>[23,24]</sup>

$$\begin{bmatrix} F_h \\ T_h \end{bmatrix} = \begin{bmatrix} A_h & 0 \\ 0 & C_h \end{bmatrix} \begin{bmatrix} U \\ \Omega_h \end{bmatrix}, \quad (8)$$

$$\begin{bmatrix} F_t \\ T_t \end{bmatrix} = \begin{bmatrix} A_t & -B_t \\ -B_t & C_t \end{bmatrix} \begin{bmatrix} U \\ \Omega_t \end{bmatrix}, \quad (9)$$

where subscriptions ‘‘h’’ and ‘‘t’’ represent the head and tail, respectively.

The model is completed by including the force- and torque-free conditions, as well as constant motor torque assumption

$$F_t = -F_h, \quad (10)$$

$$T_t = -T_h, \quad (11)$$

$$T_{\text{sw}} = T_t \equiv 1. \quad (12)$$

Solving Eqs. (8)–(12) simultaneously, the forward velocity of the microswimmer in the pipe  $U$  reads as

$$U = \frac{B_t}{(A_h + A_t)C_t - B_t^2}. \quad (13)$$

The rotation–translation coupling term of the tail  $B_t$  is an order smaller than other resistance coefficients.<sup>[25,26]</sup> Ignoring the higher-order terms  $O(B_t^2)$ , we have

$$U = \frac{F_{\text{th}}}{A_{\text{sw}}}, \quad (14)$$

where  $F_{\text{th}} = B_t/C_t$ , and  $A_{\text{sw}} = A_h + A_t$ . One can observe that the forward velocity of the microswimmer is a result of the competition between the thrust  $F_{\text{th}}$  of the tail and the total drags  $A_{\text{sw}}$  of the microswimmer. A similar relation for swimming in free space and the speed ratio can be computed as

$$\alpha = \frac{U^\infty}{U} = \frac{F_{\text{th}}^\infty A_{\text{sw}}^\infty}{F_{\text{th}} A_{\text{sw}}}, \quad (15)$$

where the superscript  $\infty$  indicates the quantities in the free space.

## 2.6. Obtain the coefficients of the resistance matrix

A crucial step to calculate the speed ratio  $\alpha$  from Eq. (15) is determining the resistance coefficients. These coefficients can be obtained from Eqs. (8) and (9) by using the Stokeslets method solving two cases: pure translation  $\{U = 1, \Omega_i = 0\}$ , and pure rotation  $\{U = 0, \Omega_i = 1\}$  for the head and the tail, respectively.

### 2.6.1. Resistance coefficients of head

The coefficients for the head in the confinement increase linearly with the length when the head is sufficiently long such that the interaction between the head and nearby pipe surface dominates (Fig. 4). When the radius of the head is small and short, the confinement effect is weak and a sub-linear (logarithmic) relation is observed. To highlight such transition, we use a relatively small radius  $r_h/R = 0.1$  in Fig. 4. As the purpose of developing the reduced model is for long head and tail cases, we approximate the forces on the head with linear functions

$$A_h = a_h l_h, \quad (16)$$

$$C_h = c_h l_h. \quad (17)$$

Quantitatively, our simulation results agree well with the analytical solutions of an infinite cylinder moving inside a pipe:<sup>[27]</sup>

$$a_h = \frac{-2\pi[1 - 4(\frac{r_h}{R})^2 - 4(\frac{r_h}{R})^4 \ln(\frac{r_h}{R}) + 3(\frac{r_h}{R})^4]}{(1 - (\frac{r_h}{R})^4) \ln(\frac{r_h}{R}) + (1 - (\frac{r_h}{R})^2)^2}, \quad (18)$$

$$c_h = \frac{4\pi r_h^2}{1 - (\frac{r_h}{R})^2}. \quad (19)$$

Then the coefficients can be used to extrapolate the resistance of long heads. We note that the effect of the pipe confinement to the rotational coefficient is much weaker than the effect on the translation coefficient (Fig. 4(b)).

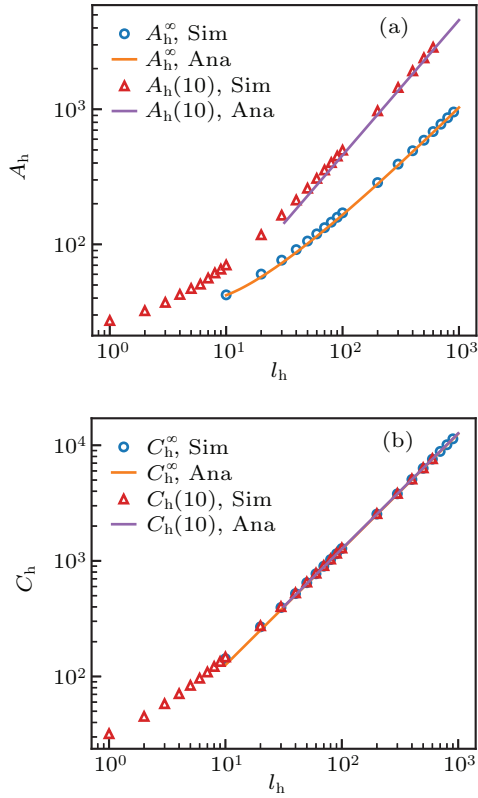


**Fig. 4.** Translational and rotational resistance coefficients of a head in free space ( $A_h^\infty$  and  $C_h^\infty$ ), and inside the pipe with radius  $r_h/R = 0.1$  ( $A_h$  and  $C_h$ ). Here  $r_h = 1$ . Solid lines represent the analytical solutions given by Eqs. (16) and (17) (in a pipe), and Eqs. (23) and (21) (in bulk fluid).

For the head in free space, we observed a linear relationship for the rotational coefficient (Fig. 4(b)). Chwang and Wu<sup>[28]</sup> presented the analytical expression of the torque per unit length of an infinitely long cylinder

$$C_h^\infty = c_h^\infty l_h, \quad (20)$$

where  $c_h^\infty = 4\pi r_h^2$ .

Thus, the rotational resistance coefficient  $C_h^\infty$  keeps the linear relationship as functions of head length  $l_h$  both inside and outside the pipe

$$c_h^\infty = \lim_{R \rightarrow \infty} c_h = 4\pi r_h^2. \quad (21)$$

In contrast, we observed a sub-linear relationship of the resistance coefficients in the forward direction (Fig. 4(a)). The

head drags  $A_h^\infty$  in the bulk fluid can not be obtained by taking a limit of Eq. (18). For very large pipe radius  $R \gg r_h$ , Eq. (18) gives

$$\lim_{R \gg r_h} A_h = 2\pi \frac{l_h}{\ln(R/r_h) - 1} + O\left(\frac{r_h}{R}\right)^2. \quad (22)$$

Alternatively, we can obtain the analytical expression for the head drag based on Ref. [29], in which the drag of a slender body of revolution is provided. Using a constant radius along axis and correcting some typos, the drag on the head is

$$A_h^\infty = a_h^\infty \frac{l_h}{\ln(l_h/r_h) + \beta_h}, \quad (23)$$

where  $a_h^\infty = 2\pi$  and  $\beta_h = \ln 2 - 3/2$ .

While Eqs. (22) and (23) look different, they are actually consistent. There is a competition between the interaction between the pipe and the interaction between different parts of the rod. When the pipe boundary is closer to the head, i.e.,  $R \ll l_h$ , the confinement effect dominates and the drag increases linearly with length; when the pipe boundary is far from the head, i.e.,  $R \gg l_h$ , the interaction between different parts of the head dominates and the drag increases sub-linearly with length. The analysis highlights the different trends of head drag with and without confinement, and in the next section, we will show the impact of this difference on the speed ratio.

## 2.6.2. Resistance coefficients of the tail

From the numerical simulation, we found that the resistance coefficients for short tail increase rapidly, and then the increase becomes slower (Fig. 5). By taking the tail pitch  $\lambda = 2.5$  as an example, we observed a local maximum of  $B_t^\infty$  near  $n_1 \approx 0.5$  ( $l_t \approx 1.25$ ). Such a maximum is the result of the shadowing of the front part of a helical tail to the posterior part, similar to a previous study.<sup>[30]</sup> The previous study showed that the speed of the microswimmer with a single helical tail peaks around one period  $n_1 \approx 1$ . Since we employed a double-helical tail, the overlap of the projection of the tail perpendicular to the forward direction occurs when  $n_1 = 0.5$  and causes the local maximum.

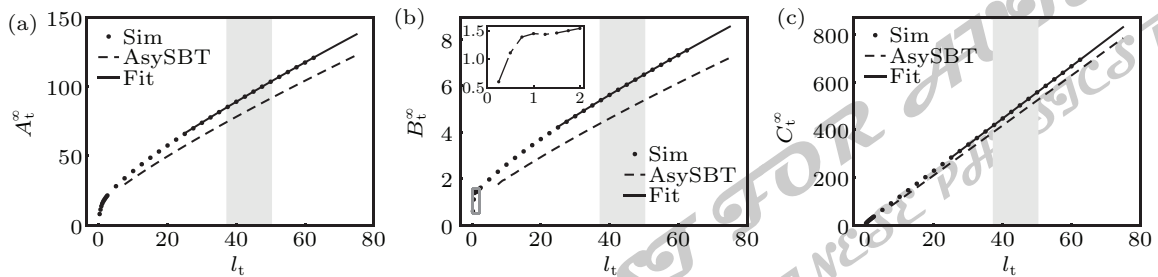


**Fig. 5.** A comparison of the resistance coefficients from the simulation, asymptotic SBT and fitting methods. The translational (a), rotational (b) and coupling (c) resistance coefficients of tail in free space as functions of tail length  $l_t$ . The inset of panel (b) reports a detailed view of the regions enclosed by the grey dotted box. Tail pitch  $\lambda = 2.5$ , tail radius  $r_t = 1$ , and flagella radius  $\rho_t = 0.1$ . The gray bars in the background indicate the range where the fittings of  $c_{ij}$  were done.

To model long tails that require too much computational power and obtain a better understanding of the resistance, we computed the coefficients for infinitely long tails and used these coefficients to approximate the coefficients for long but finite tails. For an infinitely long tail moving along or rotate about its axis, the force is uniform and symmetric about the helix axis. We use the uniform force density to connect the motion of the tail and the total force on the tail. Without loss of generality, we consider a point on one of the helix at  $\mathbf{x}_0 = (0, r_t, 0)$  (see Fig. 6). At this point, the pure translation of the double-helix leads to a local velocity  $\mathbf{u}_t = (0, 0, 1)$  and the pure rotation with an angular speed of 1 corresponds to a local velocity  $\mathbf{u}_t = (0, r_t, 0)$ .

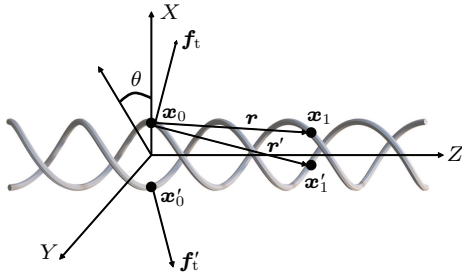


**Fig. 6.** Diagram of the infinite double helix for tail coefficient computation. The angle in  $XY$  plane  $\theta \in (-\pi, +\pi)$  is used to locate a pair of points  $(\mathbf{x}_1(\theta))$  and  $(\mathbf{x}'_1(\theta))$  on the double helix. Their displacements to  $\mathbf{x}_0$  are  $\mathbf{r}(\theta)$  and  $\mathbf{r}'(\theta)$ , respectively.

The force density is a constant in cylindrical coordinates:  $\mathbf{f}_t = (f_r, f_\theta, f_z)$ . Then the total force over one wavelength of the double-helix is

$$\mathbf{F} = (0, 0, 2nSf_z), \quad (24)$$

where  $S = \sqrt{4\pi^2 r_t^2 + \lambda^2}$  is the arc length of the helix per wavelength.

Similarly, we can calculate the total torque on the tail as a function of the force density

$$\mathbf{T} = (0, 0, 2nSf_\theta r_t). \quad (25)$$

For a constant force distribution, the velocity at the position  $\mathbf{x}_0$  can be computed using Lighthill's slender body theory (SBT)<sup>[31]</sup>

$$\mathbf{u}_t(\mathbf{x}_0) = \mathbf{M}(l_t) \mathbf{f}_t, \quad (26)$$

$$\mathbf{M} = \begin{bmatrix} c_{rr} & 0 & 0 \\ 0 & c_{\theta\theta} & c_{\theta z} \\ 0 & c_{\theta z} & c_{zz} \end{bmatrix} + \begin{bmatrix} 0 & 0 & 0 \\ 0 & 0 & 0 \\ 0 & 0 & \frac{S \ln(l_t/r_t)}{\lambda \pi} \end{bmatrix}. \quad (27)$$

The resistance matrix  $\mathbf{M}$  of the asymptotic theory is a combination of two parts. The first part comes from the contribution of the local forces, and  $c_{ij}$  are the coefficients. Due to symmetry, the cross-terms related to  $f_r$  are zero. Further, since  $c_{rr}$  is not related to translation along the axis of rotation about the axis, it is not used hereafter. The second part is the long-range

contribution of the forces. Since the displacement is dominantly along the axis and the leading term of the coefficient decays as  $1/r$ , only the component along the axis remains, and this term increases logarithmically with the tail length similar to a cylinder. See Appendix A for details of the derivation of the asymptotic analysis.

From Eq. (9) and (24)–(27), we obtained the coefficients for a long tail in free space

$$A_t^\infty = a_t^\infty \frac{l_t}{\ln(l_t/r_t) + \beta_t}, \quad (28)$$

$$B_t^\infty = b_t^\infty \frac{l_t}{\ln(l_t/r_t) + \beta_t}, \quad (29)$$

$$C_t^\infty = c_t^\infty l_t, \quad (30)$$

$$a_t^\infty = 2\pi, \quad (31)$$

$$b_t^\infty = 2\pi r_{t1} \frac{c_{\theta z}}{c_{\theta\theta}}, \quad (32)$$

$$c_t^\infty = \frac{2r_{t1}^2 S}{c_{\theta\theta}} \frac{c_{zz} \lambda \pi + \ln(l_t \pi / \lambda) S}{\left(c_{zz} - \frac{c_{\theta z}^2}{c_{\theta\theta}}\right) \lambda \pi + \ln(l_t \pi / \lambda) S} \approx \frac{2r_{t1}^2 S}{c_{\theta\theta}}, \quad (33)$$

$$\beta_t = \left(c_{zz} - \frac{c_{\theta z}^2}{c_{\theta\theta}}\right) \frac{\lambda \pi}{S} + \ln \pi - \ln \lambda. \quad (34)$$

While the coefficients in  $\mathbf{M}$  can be computed using the asymptotic SBT and an overall agreement between the theory and simulation is observed, there are quantitative discrepancies (Fig. 5). We attribute the discrepancies to the end effects and approximations in SBT such as the slenderness of the helix. Therefore, instead of using the values from asymptotic SBT, we fit the simulation data using the functional forms of Eqs. (28)–(34). This fitting allows us to approximate the resistance coefficients for longer tails.

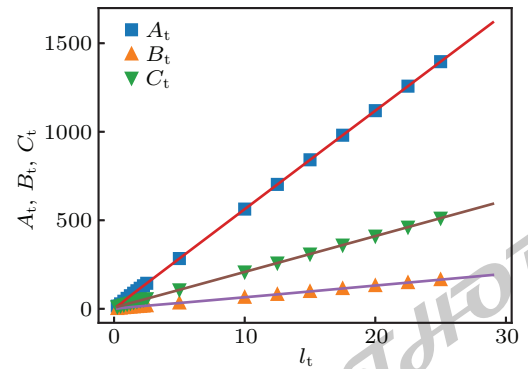


**Fig. 7.** The resistance coefficients of the tail in a pipe as functions of tail length.  $R = 1/0.7$ ,  $\lambda = 2.5$ , and  $\rho_t = 0.1$ . The solid lines show the associated linear fitting.

Due to the shielding of the long-range interaction in the pipe, the resistance coefficients for the tail increase linearly with the tail length, i.e.,

$$A_t = a_t \left(\frac{r_t}{R}\right) l_t, \quad (35)$$

$$B_t = b_t \left(\frac{r_t}{R}\right) l_t, \quad (36)$$

$$C_t = c_t \left(\frac{r_t}{R}\right) l_t. \quad (37)$$

We fit the simulation results to obtain the coefficients (see Fig. 7) and use those values for long tails. Similarly, the accuracy of the linear relationship depends on the length of the tail relative to the radius of the pipe. Since we consider tails that are close to the boundary ( $r_t/R = 0.7$ ), the linear relationship is valid for even small lengths.

### 2.6.3. Error due to the hydrodynamic decoupling

We further tested the reduced model and evaluated the error due to the decoupling using the full numerical simulations. We chose two microswimmers. One has a long head, and the other has a short head. We varied the distance be-

tween the head and tail and compared the results from the reduced model with those from the direct simulation (Fig. 8). We found that the velocities in general decrease with an increase in the gap length. We attribute the decrease to the shielding effect,<sup>[32]</sup> which reduces the drag of the microswimmer with a small head–tail gap. For all the cases, the discrepancy between the reduced model and direct simulation is small ( $< 10\%$ ), and the velocities converge for a head–tail distance  $\delta_{ht}$  greater than about 20. Since the speed ratio measures the relative value between the velocities, the variation in  $\alpha$  is amplified, and more significant changes  $\approx 20\%$  are observed as  $\delta_{ht}$  varies. Nonetheless, it converges for  $\delta_{ht} > 20$ .

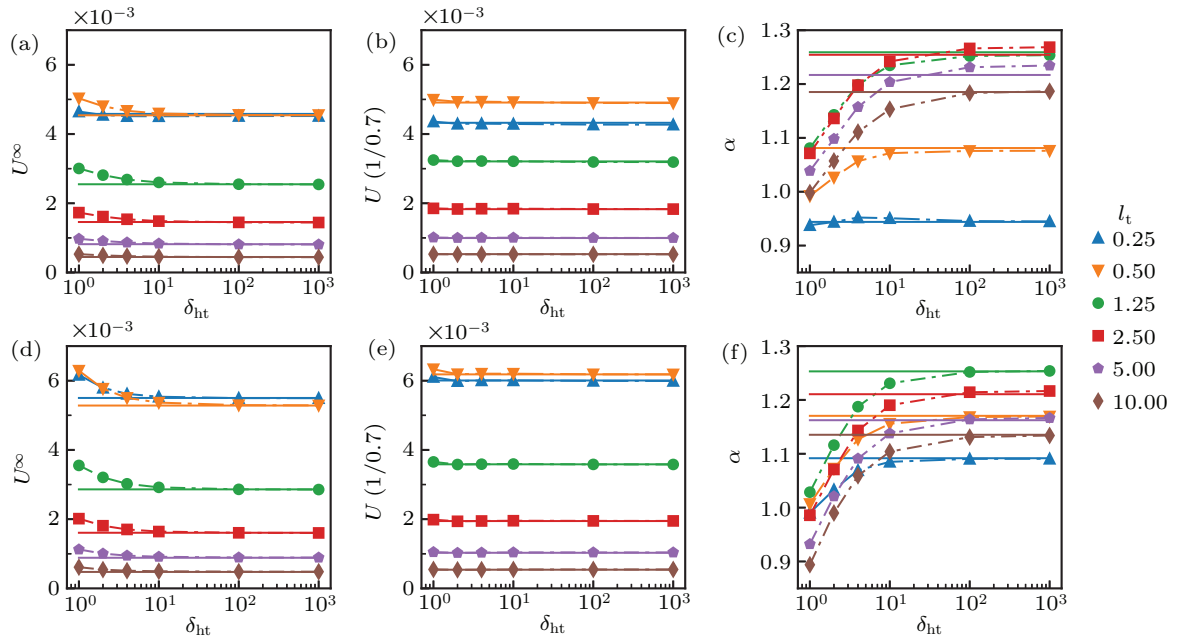


**Fig. 8.** Error due to the decoupling of the head and tail for a long head  $l_h = 1.8$  swimmer (top row) and a short head  $l_h = 0.6$  swimmer (bottom row). The velocities in free space  $U^\infty$  (a), (d) and in the pipe  $U(1/0.7)$  (b), (e) of the microswimmers, as well as their ratio  $\alpha$  (c), (f) as functions of the distance between head and tail  $\delta_{ht}$ . The solid lines correspond to the values from the reduced model, the symbols correspond to direct simulations, and the lines are drawn to guide the eye.  $r_h = 0.3$ ,  $\lambda = 2.5$ ,  $r_t = 1$ ,  $\rho_t = 0.1$ .

In the rest of the study, we combined the numerical method and reduced model to calculate the swimming speeds and speed ratios. Specifically, for short head  $l_h \leq 80$  and short tail  $l_t \leq 25$ , we employed the numerical method, and for large head  $l_h > 80$  and tail  $l_t > 25$ , we employed the reduced model.

## 3. Model prediction

To better understand the dependence of the speed ratio on the geometry, we developed analytical approximations of the speed ratio  $\alpha$  at the long head and tail limit. First, we summarize the approximations of the resistance coefficients for very long head/tail in Table 2. The resistance coefficients increase linearly in the pipe and logarithmically in free space except for the rotational resistance, which increases linearly with length both inside the pipe and in the free space. Substitute the resistance coefficients in Eq. (15) with those approximations in

Table 2, the speed ratio of the microswimmer becomes

$$\alpha = \frac{b_t c_t^\infty a_h^\infty \frac{l_h/\ln(l_h/r_h)}{l_t/\ln(l_t/r_t)} + a_t^\infty}{b_t^\infty c_t} \frac{l_t}{a_h l_h/l_t + a_t}. \quad (38)$$

Equation (38) indicates that the lengths of the head and the tail appear in pairs and have opposite effects on the ratio.

**Table 2.** The approximations of the resistance coefficients of the microswimmer.

Free space	In pipe
$A_h^\infty = a_h^\infty \frac{l_h}{\ln(l_h/r_h) + \beta_h} \approx a_h^\infty \frac{l_h}{\ln(l_h/r_h)}$	$A_h = a_h \left(\frac{r_h}{R}\right) l_h$
$A_t^\infty = a_t^\infty \frac{l_t}{\ln(l_t/r_t) + \beta_t} \approx a_t^\infty \frac{l_t}{\ln(l_t/r_t)}$	$A_t = a_t \left(\frac{r_t}{R}\right) l_t$
$B_t^\infty = b_t^\infty \frac{l_t}{\ln(l_t/r_t) + \beta_t} \approx b_t^\infty \frac{l_t}{\ln(l_t/r_t)}$	$B_t = b_t \left(\frac{r_t}{R}\right) l_t$
$C_t^\infty = c_t^\infty l_t$	$C_t = c_t \left(\frac{r_t}{R}\right) l_t$

### 3.1. The optimal geometry for the speed ratio

We first consider the microswimmers with given body slenderness (length/radius). Since many microswimmers have slenderness in the range of 1–100,<sup>[33]</sup> we used head slenderness of 10 and varied the length of the tail and head.

We observed that moderate head and tail lengths lead to the greatest speedup (Fig. 9). Due to the peak of the thrust at  $n_1 \approx 0.5$  (corresponding to  $l_t \approx 1.25$ ), the maximum of speed ratio ( $\approx 1.3$ ) also occurs near such value for the  $l_h/r_h = 10$  case. For a more slender head  $l_h/r_h = 100000$  (Fig. 9(b)), the maximal speed ratio is much larger ( $\approx 7$ ) and the peak is shifted to longer tail length.

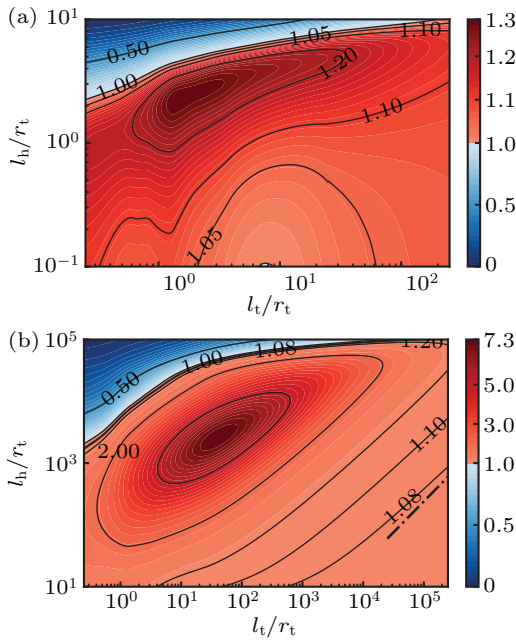


**Fig. 9.** Speed ratio  $\alpha$  as a function of the tail length and the head length normalized to the tail radius. Head slenderness,  $l_h/r_h = 10$  in (a) and  $l_h/r_h = 100000$  in (b), is kept a constant in respective subfigures. Tail pitch  $\lambda = 2.5$  and pipe radius  $R = 1/0.7$ .

We now show that the speedup phenomenon favors a moderate length ratio for both head  $l_h$  and tail  $l_t$  by considering two extreme cases inside the pipe. At the long head limit, i.e.,  $l_t \ll l_h$ , the head drag  $A_h$  is much larger than the tail drag  $A_t$  both inside and outside the pipe, even the head radius might be much smaller than the tail. Then the expression of the speed ratio can be simplified as

$$\lim_{l_t \ll l_h} \alpha \approx \frac{b_t c_t^\infty a_h^\infty}{b_t^\infty c_t a_h} \frac{\ln(l_t/r_t)}{\ln(l_h/r_h)}. \quad (39)$$

As shown in Eq. (39), the speed ratio increases with increasing tail length. Since the related term  $\ln(l_t/r_t)$  comes from the propulsion coefficient  $B$ , the physical explanation of this increase is that the increase of propulsion is faster (linear) in the pipe than that in the free space, while the increase of the tail drag is negligible. Correspondingly, the head drag exhibits the opposite behavior.

On the other hand, at the long tail limit  $l_t \gg l_h$ , where the drag contributions from the head (i.e., the terms start with  $a_h^\infty$  and  $a_h$  in Eq. (38)) are negligible. The speed ratio becomes

$$\alpha = \frac{b_t c_t^\infty a_t^\infty}{b_t^\infty c_t a_t}. \quad (40)$$

Physically, this formula corresponds to the speedup of only tails in the pipe and is in agreement with Ref. [13]. In this formula, the head drag is totally neglected. To show the influence of the head geometry, we further consider the leading order of the head drag by expanding Eq. (38). Note that since  $a_h^\infty$  and  $a_h$  are both in the order of 1,  $a_h^\infty \frac{l_h/\ln(l_h/r_h)}{l_t/\ln(l_t/r_t)}$  is much greater than  $a_h l_h/l_t$  when  $l_t \gg l_t$ . Then, we have

$$\lim_{l_t \gg l_h} \alpha \approx \frac{b_t c_t^\infty}{b_t^\infty c_t} \left( \frac{a_t^\infty}{a_t} + \frac{a_h^\infty l_h/\ln(l_h/r_h)}{a_t l_t/\ln(l_t/r_t)} \right). \quad (41)$$

Equation (41) shows that the speed ratio decreases as the tail length increases for very long tails, which agrees with the results from the reduced model (Fig. 9). As a result, the greatest speedup occurs at moderate lengths for both the head and the tail.

For  $l_h \gg 1$  and  $l_t \gg 1$ , the variations of the logarithmic terms are small and the speed ratio is approximately a constant for the same value of  $l_h/l_t$ . Therefore, the contour line in this regime is approximately straight with a slope of 1 (see the right lower corner of Fig. 9(b)). The influence of the head radius can also be seen from Eq. (41). When the tail is very long, and the head radius is small, the increase of the head radius leads to a perturbation that increases the speed ratio. When the head radius is large enough, the gap between the head and the pipe is tinny. The lubrication theory predicts that the drag force diverges.<sup>[27]</sup> Therefore, the speed ratio is maximized with a small but finite head radius.

### 3.2. Upper limit of the speed ratio

Obviously, the lower bound of the speed ratio is zero. For example, a microswimmer with a thick head can move in the free space but will get stuck in the pipe. In this subsection, we vary the slenderness of the head and discuss the maximal value of the speed ratio. We will show that the speed ratio has no upper bound by constructing certain geometries of the swimmer and associated analytical expression of the speed ratio. The key is to make the head drag much larger than the tail drag in the bulk fluid and keep the head drag comparable with the tail drag in the pipe.

The geometric relations we found are  $r_h = l_h^{-1}$  and  $l_t = l_h^{1-\eta}$ , where  $\eta = \ln(\ln l_h)/\ln l_h$ . With these geometric relations and using the approximation Eq. (22) for a very thin head, we derived the velocities and the speed ratio as follow:

$$U|_{l_h \gg R} \approx 2 \frac{b_t^\infty}{a_h^\infty c_t^\infty} l_h^{-1}, \quad (42)$$

$$U|_{l_h \gg R} \approx \frac{b_t}{(a_h^\infty + a_t) c_t} l_h^{\eta-1}, \quad (43)$$

$$\alpha|_{l_h \gg R} \approx \frac{1}{2} \frac{b_t c_t^\infty}{b_t^\infty c_t} \frac{a_h^\infty}{a_h^\infty + a_t} l_h^\eta. \quad (44)$$

Note that, even  $\lim_{l_h \rightarrow \infty} \eta = 0$ , since  $\lim_{l_h \rightarrow \infty} \ln l_h^\eta = \lim_{l_h \rightarrow \infty} \ln(\ln l_h) = \infty$ , we still have  $\lim_{l_h \rightarrow \infty} l_h^\eta = \infty$ . Therefore, the speed ratio of the microswimmer has no upper bound. Note that the optimal speed ratio for given head length can be higher than this specified shape.

The growth rate of the speed ratio, however, is very slow,  $\alpha \propto \ln l_h$  (note that  $\ln \alpha \propto \eta \ln l_h = \ln(\ln l_h)$ ), as shown in Fig. 10. Moreover, the forward velocity decreases as  $U \sim l_h^{-1} \propto \exp(-\alpha)$  at the very long head limit. Thus, even the speed ratio is huge, the microswimmer with such kind of geometry almost can not move forward. Therefore, the large speed ratio has little use to practical artificial systems and biological systems, as the head aspect ratios of most bacteria are on the order of magnitude  $10^0$  to  $10^2$ .<sup>[33]</sup>

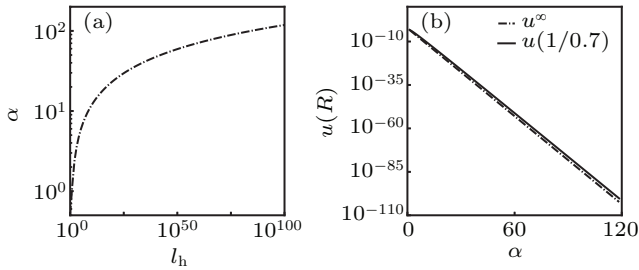


**Fig. 10.** (a) The speed ratio as a function of head length  $l_h$  when the head radius varies as  $r_h = l_h^{-1}$  and tail length varies as  $l_t = l_h^{1-\eta}$ . (b) The velocities inside the pipe and in free space as functions of the speed ratio.

### 3.3. Influence of the motor output characteristics

The motor output characteristics (speed–torque relation) affect the spin speed of the tail  $\Omega_t$ . The different spin speeds can lead to different thrusts and affect the speed ratio. In general, the torque stays a constant or decreases as the speed increases. Therefore, we consider three cases: constant torque, constant frequency (spin), and constant power. As shown in Table 3, in the constant torque case, the spin of the tail is simply  $\Omega_t = 1/C_t$  and  $\Omega_t^\infty = 1/C_t^\infty$ , and their ratio  $C_\Omega^T = c_t^\infty/c_t$  appeared in Eq. (38). For the constant-frequency case, the constant spin speed is distributed to the tail and the head according to the proportion of the total rotational resistance and that results in a ratio  $C_\Omega^f = \frac{c_h c_h^\infty l_h/l_t + c_t^\infty}{c_h^\infty c_h l_h/l_t + c_t}$ . Taking the advantage of the linear relationship of the velocities and forces, the swimming speed ratio  $\alpha$  can be obtained by scaling of the results from the constant torque case, i.e.,

$$\alpha_f = C_\Omega^f / C_\Omega^T \alpha = \frac{1/C_t^\infty + 1/C_h^\infty}{1/C_t + 1/C_h} \alpha. \quad (45)$$

Since the resistance coefficients in the pipe are always greater than those in free space, it is easy to see that  $\alpha_f > \alpha$ .

As show in Fig. 11, the overall profile is similar to the constant torque case (Fig. 9). As the power is the product of spin speed and torque, the case of constant power can be considered as an average of the constant-frequency and constant

torque cases. Therefore, for some swimmers, at least including those with  $\alpha > 1$  in Fig. 9, the cost of transport in terms of energy consumption per distance is lower in the pipe than that in the free space.

**Table 3.** Influence of motor output characteristics on the spin speeds of the tail and their ratio.

	Constant torque ( $T$ )	Constant frequency ( $f$ )	Constant power ( $P$ )
$\Omega_t^\infty$	$\frac{1}{C_t^\infty}$	$\frac{C_h^\infty}{C_h^\infty + C_t^\infty}$	$\sqrt{\frac{1}{C_t^\infty} \frac{C_h^\infty}{C_h^\infty + C_t^\infty}}$
$\Omega_t$	$\frac{1}{C_t}$	$\frac{C_h}{C_h + C_t}$	$\sqrt{\frac{1}{C_t} \frac{C_h}{C_h + C_t}}$
$C_\Omega = \Omega_t / \Omega_t^\infty$	$\frac{c_t^\infty}{c_t}$	$\frac{c_h c_h^\infty l_h/l_t + c_t^\infty}{c_h^\infty c_h l_h/l_t + c_t}$	$\sqrt{\frac{c_t^\infty c_h c_h^\infty l_h/l_t + c_t^\infty}{c_t c_h^\infty c_h l_h/l_t + c_t}}$

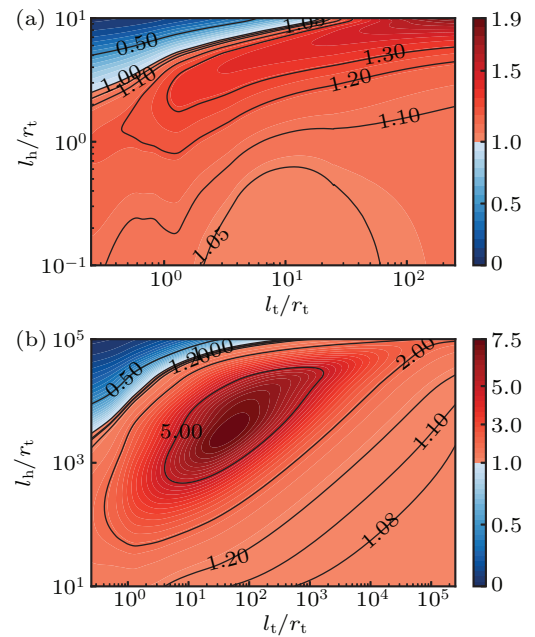


**Fig. 11.** Speed ratio as a function of the tail length and head length. Motor spin speed  $\Omega_{sw}$  is a constant 1. Head slenderness,  $l_h/r_h = 10$  in (a) and  $l_h/r_h = 100000$  in (b), is kept a constant in respective subfigures. Tail pitch  $\lambda = 2.5$  and pipe radius  $R = 1/0.7$ .

## 4. Conclusion

In this study, we investigated the speedup of microswimmers in a confined environment — an infinitely long pipe. Using numerical simulation and robotic experiments, we showed that a free swimmer can speedup in such confinement purely due to hydrodynamic effects. By developing a reduced model and analyzing the propulsion and drag forces on the head and tail, we showed that the speed ratio is maximized by a moderately long head and tail. While the speedup for a swimmer with realistic geometry is small, theoretically, the speed ratio has no upper limit when the lengths of the head and tail increase with a certain proportion and head slenderness. Our results highlight the shielding effect on the interactions between different parts of the swimmer. Such a mechanism might also influence the locomotion in other confined environments. We also showed that the virtual motor that generates a constant

frequency could lead to a greater speedup compared with a virtual motor that can generate a constant torque.

The bacterial tails are usually flexible. The helical shape is formed due to the coupling between the driving torque and force from the motor, internal elastic forces, and drag forces from surrounding fluids.<sup>[34–36]</sup> Our study is limited to a fixed shape to focus on the hydrodynamic effect due to the confinement. How confinements affect the shape and locomotion performance of realistic flexible tails will be studied in the future.

## Acknowledgments

Project supported by the National Natural Science Foundation of China (Grant Nos. 11672029 and U1930402). We thank Xinliang Xu, Ebru Demir, and Martin Stynes for helpful discussions and carefully reading the manuscript. We acknowledge the computational support from the Beijing Computational Science Research Center.

## Appendix A: The Stokeslets method in a pipe

First, here we recapitulate the Stokeslets method. Consider a Stokes flow with a point force  $\mathbf{f}$  located at  $\mathbf{x}_f$  in the region  $\Omega$ . The governing equation of the velocity  $\mathbf{u}$  reads as

$$\mu \Delta \mathbf{u} = \nabla p - \mathbf{f} \delta(\mathbf{x}_f), \quad (\text{A1})$$

$$\nabla \cdot \mathbf{u} = 0, \quad (\text{A2})$$

where  $p$  is the pressure, and  $\mu$  is the fluid viscosity. A Dirichlet boundary condition is prescribed at the region boundary  $\partial\Omega$ :

$$\mathbf{u}|_{\partial\Omega} = \tilde{\mathbf{u}}, \quad (\text{A3})$$

where  $\tilde{\mathbf{u}}$  is a given velocity.

The principle of the Stokeslets method is to place many known solutions of point forces on the boundary or somewhere outside  $\Omega$ , called Stokeslets  $\mathbf{S}_{kn}$ , then find the strength of these Stokeslets that generate the desired boundary velocity. One of the most commonly used Stokeslets is the one in three-dimensional infinite space:

$$\mathbf{S}(\mathbf{x}, \mathbf{x}_f) = \frac{1}{8\pi\mu} \left( \frac{\mathbf{I}}{r} + \frac{(\mathbf{x} - \mathbf{x}_f)(\mathbf{x} - \mathbf{x}_f)}{r^3} \right), \quad (\text{A4})$$

where  $r = |\mathbf{x} - \mathbf{x}_f|$  is the distance between the point force and the velocity point.

In the method of Stokeslets, boundaries are covered by  $n$  discrete points. Thus, there are  $3n$  known velocities  $\mathbf{v} = \{\mathbf{u}(\mathbf{x}_k), k = 1, \dots, n, \mathbf{x}_k \in \partial\Omega\}$  and  $3n$  unknowns  $\mathbf{g} = \{\mathbf{f}(\mathbf{x}_k), k = 1, \dots, n, \mathbf{x}_k \in \partial\Omega\}$ , and a system of  $3n$  linear equations that can be written in a matrix form

$$\begin{bmatrix} \mathbf{u}(\mathbf{x}_1) \\ \dots \\ \mathbf{u}(\mathbf{x}_n) \end{bmatrix} = \begin{bmatrix} \mathbf{S}_{kn}(\mathbf{x}_1, \mathbf{x}_1) & \dots & \mathbf{S}_{kn}(\mathbf{x}_1, \mathbf{x}_n) \\ \dots & \ddots & \dots \\ \mathbf{S}_{kn}(\mathbf{x}_n, \mathbf{x}_1) & \dots & \mathbf{S}_{kn}(\mathbf{x}_n, \mathbf{x}_n) \end{bmatrix} \begin{bmatrix} \mathbf{f}(\mathbf{x}_1) \\ \dots \\ \mathbf{f}(\mathbf{x}_n) \end{bmatrix}, \quad (\text{A5})$$

or

$$\mathbf{v} = \mathbf{M}\mathbf{g}. \quad (\text{A6})$$

The matrix equations were solved using the generalized minimal residual method (GMRES) in this study. Once the strength  $\mathbf{g}$  on the boundary is obtained, the velocity at an arbitrary location  $\mathbf{x}$  can be calculated by

$$\mathbf{u}(\mathbf{x}) = \sum_{k=1}^n \mathbf{S}_{kn}(\mathbf{x}, \mathbf{x}_k) \mathbf{f}(\mathbf{x}_k). \quad (\text{A7})$$

## Series solution of the Stokeslets in a pipe

Here we develop the Stokeslets in a pipe based on the series solution of a point force given by Liron and Shahar.<sup>[22]</sup> The velocities at the pipe boundary and infinity are zero:

$$\begin{cases} \mathbf{u}_b = 0, \\ \mathbf{u}_\infty = 0. \end{cases} \quad (\text{A8})$$

In cylindrical coordinates, the expression of the velocity at  $\mathbf{x}_u = (r, \phi, z)$  due to a point force located at  $\mathbf{x}_f = (b, 0, 0)$  in the pipe (see Fig. A1) is

$$\begin{aligned} & \mathbf{u}_{\text{pipe}}(\mathbf{x}_u) \\ &= \sum_{k=-\infty}^{\infty} \begin{pmatrix} \sin k\phi \\ \cos k\phi \end{pmatrix} \sum_{n=1}^{\infty} \begin{pmatrix} \exp(-b_{n,k}z) \mathbf{P}_{k,n}(x_{n,k}, \mathbf{x}_f) \\ + \exp(-c_{n,k}z) \mathbf{Q}_{k,n}(y_{n,k}, \mathbf{x}_f) \end{pmatrix}, \end{aligned} \quad (\text{A9})$$

where  $\mathbf{u}_{\text{pipe}} = (u_R, u_\phi, u_z)$  is the velocity vector,  $\mathbf{P}_{k,n}$  and  $\mathbf{Q}_{k,n}$  are complex functions of the modified Bessel functions of the first kind  $I_k(s)$  and the second kind  $K_k(s)$ , respectively. The details can be found in Appendix B of Ref. [22]. In Eq. (A9),  $b_{n,k} = \text{Im}(x_{n,k})$ , and  $c_{n,k} = \text{Im}(y_{n,k})$ , where  $\text{Im}(\bullet)$  means the imaginary part of  $\bullet$ .  $x_{n,k}$  and  $y_{n,k}$  are the complex and imaginary roots of Eq. (A6) in Ref. [22]:

$$sI_k(s)(I_{k-1}(s)I_{k+1}(s))' - 2(sI_k(s))'I_{k-1}(s)I_{k+1}(s) = 0. \quad (\text{A10})$$

Since  $I_k(s) = I_{-k}(s)$  when  $k \in \mathbb{Z}$ ,  $x_{n,-k} = x_{n,k}$  and  $y_{n,-k} = y_{n,k}$ . In this study, the roots of Eq. (A10) in the ranges  $k = 0-1000$  and  $n = 1-1000$  were solved and stored.

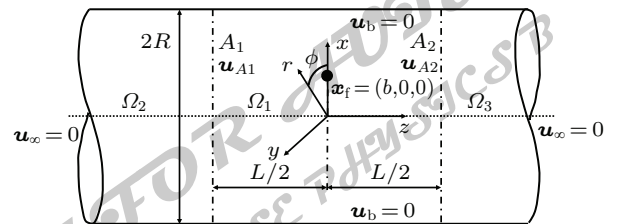


**Fig. A1.** Schematics of the Stokeslets in a pipe. A cylindrical coordinate  $(r, \phi, z)$  is employed in the system. The a dotted line represents the axis of the pipe, which coincides with the  $z$ . The point force is located at  $\mathbf{x}_f = (b, 0, 0)$ . The pipe is cut into three parts by two imaginary surfaces  $A_1$  and  $A_2$  (indicated by dash-dotted lines) and are labeled as  $\Omega_1$ ,  $\Omega_2$  and  $\Omega_3$ . The regions  $\Omega_2$ , and  $\Omega_3$  are semi-infinite and the length of  $\Omega_1$  is  $L$ .

Next, we examine the convergence of the series solution and show that the converges for small  $z$  are too slow to be used directly. There are two exponential decays in the series solution, and the associated coefficients are  $b_{n,k}z$  and  $c_{n,k}z$ . As shown in Fig. A2, both these two coefficients increase monotonically with  $n$  and  $k$ , but the increase with  $k$  is approximately two times faster than that with  $n$ . Therefore, we choose cutoff thresholds differently for  $k$  and  $n$  such that values of the last components  $b_{n,k}$  and  $c_{n,k}$  are approximately the same to avoid the useless computation. As shown in Figs. A2(c) and A2(d), with the same cutoff value  $C_{th}$ , the values for  $b_{n,k}$  and  $c_{n,k}$  are about the same. Then the infinite series become

$$\mathbf{u}_{\text{pipe}}(\mathbf{x}_u, C_{th}) = \sum_{k=-C_{th}}^{C_{th}} \begin{pmatrix} \sin k\phi \\ \cos k\phi \end{pmatrix} \sum_{n=1}^{\lfloor (C_{th}-|k|)/2 \rfloor} \begin{pmatrix} \exp(-b_{n,k}z) \mathbf{P}_{k,n}(x_{n,k}, \mathbf{x}_f) \\ + \exp(-c_{n,k}z) \mathbf{Q}_{k,n}(y_{n,k}, \mathbf{x}_f) \end{pmatrix}, \quad (\text{A11})$$

where  $\lfloor x \rfloor$  stands for the integer  $n$  satisfying  $n \leq x < n+1$ .

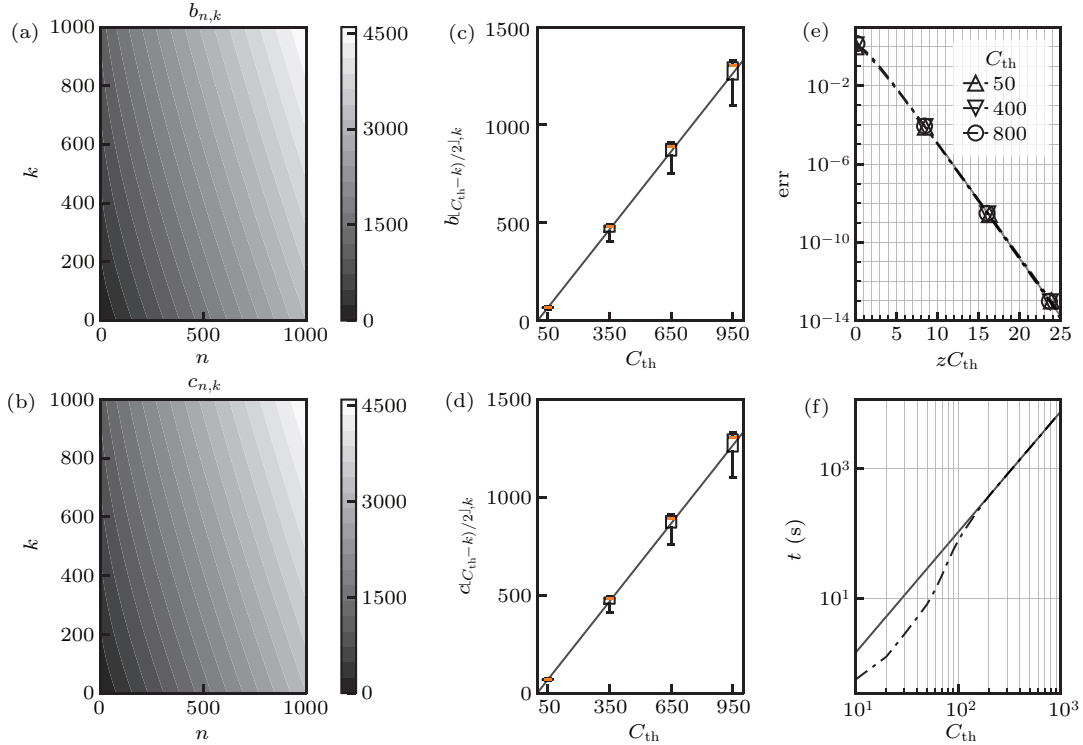


**Fig. A2.** Convergence test of the Stokeslets in a pipe. (a) and (b) The contour plots of  $b_{n,k}$  and  $c_{n,k}$  as functions of  $n$  and  $k$ , respectively. (c) and (d) The values of  $b_{n,k}$  and  $c_{n,k}$  as functions of the cutoff value  $C_{th}$ , respectively. (e) The error of the velocity at different positions and cutoff parameters. The solid line, with a slope of  $-1.3648$ , is the best linear fit of the data. (f) The time required for computing the series expression. The solid line is the best linear fit of the data, and its slope is 1.87.

A point force  $\mathbf{f} = (0, 0, 1)$  located at  $\mathbf{x}_f = (0.5R, 0, 0)$  is selected in the test. We chose the velocity value from  $C_{ref} = 1000$  as the reference solution and the relative error for cutoff  $C_{th}$  is computed as

$$\text{err}(r, \phi, z, C_{th}) = \sqrt{\sum_{i,j=1,2,3} \left( \frac{u_j^i(r, \phi, z, C_{ref}) - u_j^i(r, \phi, z, C_{th})}{u_j^i(r, \phi, z, C_{ref})} \right)^2}. \quad (\text{A12})$$

We vary the distance  $z$  and cutoff threshold  $C_{th}$  and the error is shown in Fig. A2(e). By fitting straight lines in the semilog plot, we find that the error follows the relationship

$$\text{err} = 0.87 \exp(-1.38zC_{th}). \quad (\text{A13})$$

Therefore, for given  $\text{err}$  and  $z$ , the required  $C_{th}$  is

$$C_{th} = \frac{\ln(\text{err}/0.87)}{-1.38z}. \quad (\text{A14})$$

The computational cost includes two parts: obtaining the roots of Eq. (A10), and the summation in Eq. (A11). Since the roots can be solved just once and stored, the only time-consuming part of the computation is the summation. The average time to compute 1000 times of  $\mathbf{S}_{\text{pipe}}$  on a computer with Intel(R) Xeon(R) CPU E5-2680 v3 @ 2.50 GHz is shown in Fig. A2(f). We observed that the time increases near quadratically with  $C_{th}$ . If we set a goal for the maximal error as  $\text{err} = 10^{-3}$ , the computational time required for  $z = 0.01R$  and  $z = 0.001R$  is 98 seconds and more than two hours, respectively. As we need to cover the surface of the whole body with the Stokeslets, such time consumption is unacceptable.

### Reconstruct the Stokeslets in pipe

In this section, an analytical–numerical combined method is used to solve the small  $z$  problem raised above. As shown in Fig. A1, the pipe is cut into three regions by two planes  $A_1$  and  $A_2$ . The middle region contains the point force. The series expression converges rapidly in the other two regions and does not require special treatment. The goal is to obtain the Stokeslets  $S_{\text{pipe}}$  numerically in the middle region  $\Omega_1$ .

As a tensor,  $S_{\text{pipe}}$  can be obtained by the calculation of three orthogonal velocity components for point forces along the three axes. The boundary condition  $\tilde{\mathbf{u}}$  consists of three parts, i.e.,  $\mathbf{u}_b = 0$  on the pipe wall,  $\mathbf{u}_{A_1}$  on the imaginary wall  $A_1$ , and  $\mathbf{u}_{A_2}$  on the imaginary wall  $A_2$ . Since we can compute the velocity on  $A_1$  and  $A_2$  accurately using the series expression, their values are known.

To remove the singularity in  $\Omega_1$  and make the Stokes equation satisfied everywhere, we subtract the velocity field from a point force in free space and add it back later. The residual velocity  $\mathbf{u}_{\text{res}}^i(\mathbf{x}, \mathbf{x}_f)$  is

$$\mathbf{u}_{\text{res}}^i(\mathbf{x}, \mathbf{x}_f) = \mathbf{u}_{\text{pipe}}^i(\mathbf{x}, \mathbf{x}_f) - \mathbf{u}^i(\mathbf{x}, \mathbf{x}_f), \quad (\text{A15})$$

where  $\mathbf{u}^i(\mathbf{x}, \mathbf{x}_f) = \mathbf{S}\mathbf{f}$  is the singular velocity field due to a unit point force  $\mathbf{e}^i(\mathbf{x}_f)$  in free space (see Fig. A3(b)), The residual velocity field cancels the velocity at the pipe surface. The problem is reduced to finding the residual velocity field numerically that satisfies the boundary condition  $\tilde{\mathbf{u}}_{\text{res}}^i(\mathbf{x}_f)$  (see Fig. A3(c)). The force distribution  $\mathbf{g}_{\text{res}}$  on the boundary for this residual velocity field can be solved with the Stokeslets method.

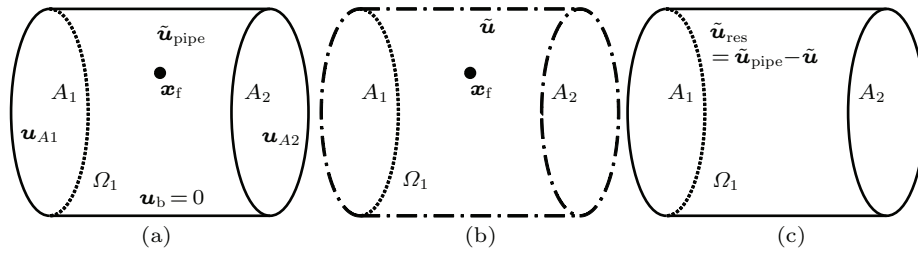


**Fig. A3.** Schematics of the numerical method for reconstructing the Stokeslets in  $\Omega_1$ . (a) The Stokes problem in a finite pipe with a singular unit point force  $\mathbf{f}$  located at  $\mathbf{x}_f$  and given boundary condition  $\tilde{\mathbf{u}}_{\text{pipe}}$ . The fluid field (Stokeslets) induced by  $\mathbf{f}$  can be decomposed into a singular part (b) and a harmonic part (c). (b) The flow induced by the Stokeslets in free space  $S$ . The velocity on the imaginary boundary is  $\tilde{\mathbf{u}}$ . (c) The Stokes problem with the boundary condition  $\tilde{\mathbf{u}}_{\text{res}} = \tilde{\mathbf{u}}_{\text{pipe}} - \tilde{\mathbf{u}}$ .

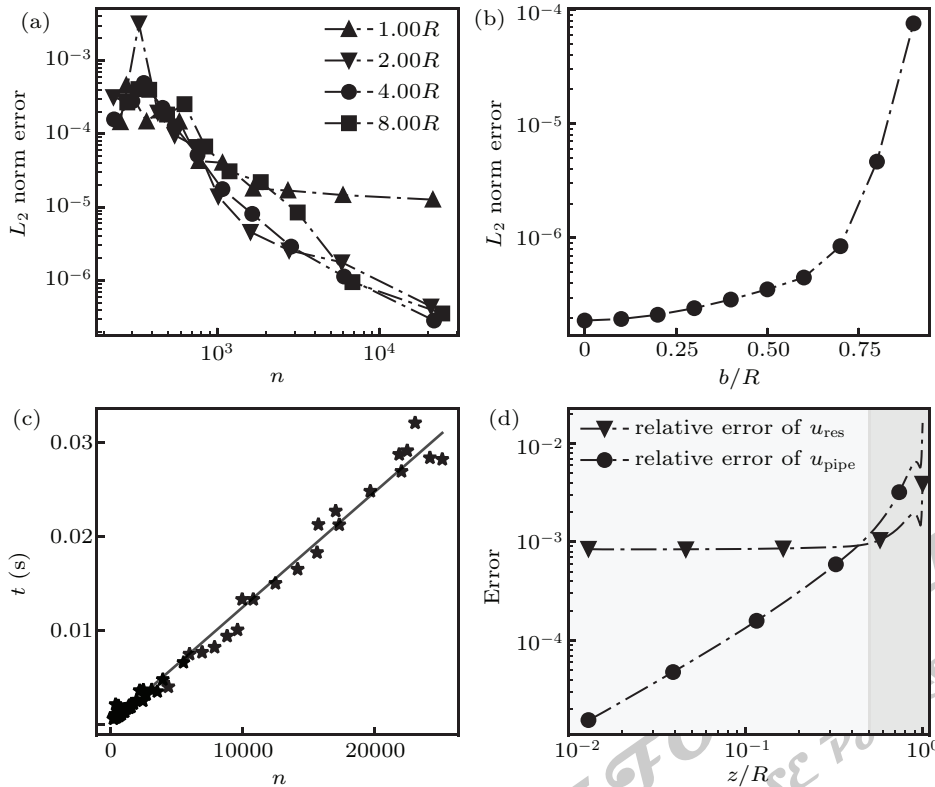


**Fig. A4.** The convergence test of the reconstructed Stokeslet. (a) The  $L_2$ -norm errors of the boundary velocity as functions with the total of the Stokeslets  $n$  on the boundary of the finite pipe  $\Omega_1$  with different lengths. In this test case, a unit point force  $\mathbf{f} = (0, 0, 1)$  is located at  $\mathbf{x}_f = (0.5R, 0, 0)$ . (b) The  $L_2$ -norm error of the boundary velocity as a function of the location  $\mathbf{x}_f = (b, 0, 0)$  of a unit point force  $\mathbf{f} = (0, 0, 1)$ . (c) The computational time of using the Stokeslets in pipe as a function of the total number of Stokeslets used on the boundary in the reconstruction process. (d) A comparison between the velocities on the line  $(0.5R, 0, z)$  computed using the series expression  $u_z^{\text{ana}}$  and using the reconstruction method  $u_z^{\text{num}}$ . The relative error of  $u_{\text{res},z}$  is computed as  $\|(u_{\text{res},z}^{\text{ana}} - u_{\text{res},z}^{\text{num}})/u_{\text{res},z}^{\text{ana}}\|$ . The relative error of  $u_{\text{pipe},z}$  is computed as  $\|(u_{\text{pipe},z}^{\text{ana}} - u_{\text{pipe},z}^{\text{num}})/u_{\text{pipe},z}^{\text{ana}}\|$ .

**Table A1.** Steps of reconstructing and using the Stokeslets in a pipe.

1. Preparation process:
(a) cut the infinite pipe into three regions,
(b) calculate the boundary velocity of the middle region using the series expression,
(c) decompose the velocity field into singular and harmonic parts (residual velocity),
(d) item solve the residual velocity and make the lookup table of strength $G_{\text{res}}^i$ .
2. Application process:
(a) interpolate $g_{\text{res}}^i(\mathbf{x}_f)$ using $G_{\text{res}}^i$ ,
(b) compute the velocity $\mathbf{u}$ for the point of interest,
(c) add back the velocities from the Stokeslet $\mathbf{S}$ to obtain $\mathbf{M}$ .

A technical problem is to find proper pipe length  $L$ . We examined the accuracy of the numerical method for different pipe lengths and the number of force points on the boundary. We placed 6000 random points on the boundary of the finite pipe  $\Omega_1$ , and calculated the  $L_2$ -norm error. As shown in Fig. A4(a), the  $L_2$ -norm error of the short pipe ( $L = R$ ) is significantly worse than other cases. This is because of the complex velocity profile on the surfaces  $A_1$  and  $A_2$ . Therefore, we chose  $L = 2R$  in this study.

The strength  $g_{\text{res}}$  for the residual field is a function of radial location of the point force. We found that the error increases significantly when  $b > 0.8$  and becomes computational demanding (Fig. A4(b)). To speedup the numerical method, we made a lookup table for  $g_{\text{res}}$ . Particularly, we computed  $g_{\text{res}}^i(\mathbf{x}_{fl})$  for a point at  $\mathbf{x}_{fl}$ , where  $\mathbf{x}_{fl} = (b_l, 0, 0)$ .  $b_l = 0, \dots, 0.8$ , where  $l = 0, 1, \dots, 800$ . The lookup table contains all solved values of the point forces is denoted as  $G_{\text{res}}^i = \{g_{\text{res}}^i(\mathbf{x}_{fl})\}$ . Then a spline interpolation was employed to calculate the strength  $g_{\text{res}}^i(\mathbf{x}_f)$  from the stored lookup table  $G_{\text{res}}^i$ . The Stokeslets  $\mathbf{S}_{\text{pipe}}$  can be reconstructed once the residual velocity fields  $\mathbf{u}_{\text{res}}^i$  are computed by adding back the Stokeslet in free space. A summation of the reconstruction process is listed in Table A1.

The computational time increases linearly with the number of Stokeslets in the reconstruction process (see Fig. A4(c)). In this study, we placed 9214 point forces on the boundary of the finite pipe  $\Omega_1$ .

To test the accuracy of the reconstructed velocity field, we placed the point force  $(0, 0, 1)$  at  $(0.5R, 0, 0)$  and calculated the relative error of  $\mathbf{u}_{\text{res}}$  and  $\mathbf{u}_{\text{pipe}}$  (Fig. A4(d)). The relative errors of  $\mathbf{u}_{\text{res}}$  are small in the range  $\|z\| < 0.5$  (light gray area in Fig. A4(d)) but increase for large  $z$  due to the discretization on the boundary. Contrary to the series expression, the reconstructed Stokeslets in pipe have higher accuracy near the point force. Therefore, the series expression of the Stokeslets was used for  $\|z\| > 0.5$ .

### Resistance coefficients of an infinitely long tail in free space

As shown in Fig. 6, we considered a double-helix moving in free space and computed the resistance coefficients for axial translation and rotation. Now we calculate the force density  $\mathbf{f}_t$

using Lighthill's slender body theory.<sup>[31]</sup> Without loss of generality, we set the viscosity of fluid  $\mu \equiv 1$  in this study. We assume that the length of the double-helix  $l_t$  is long enough such that the force density is a constant in cylindrical coordinates, i.e.,  $\mathbf{f}_t = (f_r, f_\theta, f_z)$ , and the end effects are negligible. The force on one of the helices in Cartesian coordinates can be obtained by coordinates transformation

$$\mathbf{f} = (f_x, f_y, f_z) = \mathbf{R}\mathbf{f}_t(f_r, f_\theta, f_z), \quad (\text{A16})$$

where

$$\mathbf{R}(\theta) = \begin{bmatrix} \cos \theta & -\sin \theta & 0 \\ \sin \theta & \cos \theta & 0 \\ 0 & 0 & 1 \end{bmatrix}, \quad (\text{A17})$$

$$\mathbf{R}'(\theta) = \mathbf{R}(\theta + \pi). \quad (\text{A18})$$

Then the relation between the velocity  $\mathbf{u}_t$  and force  $\mathbf{f}_t$  at  $\mathbf{x}_0 = (r_{t1}, 0, 0)$  can be computed as

$$\mathbf{u}_t(\mathbf{x}_0) = \mathbf{M}(\theta_1)\mathbf{f}_t, \quad (\text{A19})$$

$$\mathbf{M}(\theta_1) = \frac{\mathbf{I} - \hat{\mathbf{t}}_t \hat{\mathbf{t}}_t}{4\pi} + \frac{\mathbf{S}}{2\pi} \int_{r(\theta) > \delta_t} \mathbf{S}(\mathbf{x}_0, \mathbf{x}_1(\theta)) \mathbf{R}(\theta) d\theta + \frac{\mathbf{S}}{2\pi} \int_{-\theta_1}^{\theta_1} \mathbf{S}(\mathbf{x}_0, \mathbf{x}'_1(\theta)) \mathbf{R}'(\theta) d\theta, \quad (\text{A20})$$

where  $\delta_t = \rho_t \sqrt{\epsilon}/2$  is the "natural cutoff",<sup>[31]</sup>  $\theta_1 = l_t \pi / \lambda$ ,  $\mathbf{r} = \mathbf{x}_1 - \mathbf{x}_0$  ( $\mathbf{r}' = \mathbf{x}'_1 - \mathbf{x}_0$ ),  $\mathbf{x}_1$  ( $\mathbf{x}'_1$ ) is an arbitrary point on the 1<sup>st</sup> (2<sup>nd</sup>) helix, and  $\mathbf{S}$  is the Stokeslets (Oseen tensor)

$$\mathbf{S}(\mathbf{x}_0, \mathbf{x}_1) = \frac{1}{8\pi} \begin{bmatrix} \frac{1}{r} + \frac{r_x r_x}{r^3} & \frac{r_x r_y}{r^3} & \frac{r_x r_z}{r^3} \\ \frac{r_y r_x}{r^3} & \frac{1}{r} + \frac{r_y r_y}{r^3} & \frac{r_y r_z}{r^3} \\ \frac{r_z r_x}{r^3} & \frac{r_z r_y}{r^3} & \frac{1}{r} + \frac{r_z r_z}{r^3} \end{bmatrix}, \quad (\text{A21})$$

here  $r = \|\mathbf{r}\|$ .

The first term of Eq. (A20) is the local contribution of the force to the velocity, taking into account of the force singularity. Due to the symmetry, the axial motion generates no radial forces and vice versa. Therefore, there are four zeros in the  $\mathbf{M}$  matrix

$$\mathbf{M}(l_t) \equiv \begin{bmatrix} c_{rr} & 0 & 0 \\ 0 & c_{\theta\theta} & c_{\theta z} \\ 0 & c_{\theta z} & c_{zz} + \frac{\mathbf{S}}{\lambda\pi} \ln(l_t/r_t) \end{bmatrix}. \quad (\text{A22})$$

Here,  $S\ln(l_t/r_t)/(\lambda\pi)$  represents the nonlocal effects along the axial direction.

The local contribution  $c_{ij}$  of the  $M$  matrix can be integrated numerically. For instance, with  $r_t = 1$ ,  $\rho = 0.1$ , and  $\lambda = 2.5$ , we obtained  $(c_{rr}, c_{\theta\theta}, c_{\theta z}, c_{zz}) = (0.09416, 0.51779, 0.03036, 1.16631)$ .

## References

- [1] Ai Y, Xie R, Xiong J and Liang Q 2020 *Small* **16** 1903940
- [2] Alapan Y, Yasa O, Yigit B, Yasa I C, Erkoc P and Sitti M 2019 *Annual Review of Control, Robotics, and Autonomous Systems* **2** 205
- [3] Xu D, Wang Y, Liang C, You Y, Sanchez S and Ma X 2020 *Small* **16** 1902464
- [4] Troccaz J and Bogue R 2008 *Industrial Robot: An International Journal*
- [5] Magdanz V, Koch B, Sanchez S and Schmidt O G 2015 *Small* **11** 781
- [6] Liu C, Zhou C, Wang W and Zhang H P 2016 *Phys. Rev. Lett.* **117** 198001
- [7] Ledesma-Aguilar R and Yeomans J M 2013 *Phys. Rev. Lett.* **111** 138101
- [8] Katz D F 1974 *Journal of Fluid Mechanics* **64** 33
- [9] Zhu L, Lauga E and Brandt L 2013 *Journal of Fluid Mechanics* **726** 285
- [10] Lintuvuori J S, Brown A T, Stratford K and Marenduzzo D 2016 *Soft Matter* **12** 7959
- [11] Caldag H O, Acemoglu A and Yesilyurt S 2017 *Microfluidics and Nanofluidics* **21** 1
- [12] Felderhof B 2010 *Physics of Fluids* **22** 113604
- [13] Liu B, Breuer K S and Powers T R 2014 *Physics of Fluids* **26** 1
- [14] Vizsnyiczai G, Frangipane G, Bianchi S, Saglimbeni F, Dell Arciprete D and Di Leonardo R 2020 *Nat. Commun.* **11** 1
- [15] Acemoglu A and Yesilyurt S 2014 *Biophysical Journal* **106** 1537
- [16] Berg H C and Turner L 1993 *Biophysical Journal* **65** 2201
- [17] Xing J, Bai F, Berry R and Oster G 2006 *Proc. Natl. Acad. Sci. USA* **103** 1260
- [18] Young D L, Jane S J, Fan C M, Murugesan K and Tsai C C 2006 *Journal of Computational Physics* **211** 1
- [19] Zhang J, Chinappi M and Biferale L 2021 *Phys. Rev. E* **103** 023109
- [20] Zhao L, Zhang L and Ding Y 2018 *Physics of Fluids* **30** 032006
- [21] Zöttl A 2020 *Chin. Phys. B* **29** 074701
- [22] Liron N and Shahar R 1978 *Journal of Fluid Mechanics* **86** 727
- [23] Rodenborn B, Chen C H, Swinney H L, Liu B and Zhang H 2013 *Proc. Natl. Acad. Sci. USA* **110** E338
- [24] He-Peng Z, Bin L, Rodenborn B and Swinney H L 2014 *Chin. Phys. B* **23** 114703
- [25] Purcell E M 1977 *American Journal of Physics* **45** 3
- [26] Spagnolie S E and Lauga E 2011 *Phys. Rev. Lett.* **106** 058103
- [27] Happel J and Brenner H 1983 *Low Reynolds number hydrodynamics: with special applications to particulate media* (Heidelberg : Springer Science & Business Media) p. 341
- [28] Chwang A and Wu T 1974 *Journal of Fluid Mechanics* **63** 607
- [29] Tillett J 1970 *Journal of Fluid Mechanics* **44** 401
- [30] Shum H, Gaffney E and Smith D 2010 *Proc. Roy. Soc. A: Math. Phys. Engin. Sci.* **466** 1725
- [31] Lighthill J 1976 *SIAM Review* **18** 161
- [32] Gluckman M J, Pfeffer R and Weinbaum S 1971 *Journal of Fluid Mechanics* **50** 705
- [33] Brennen C, Winet H 1977 *Annual Review of Fluid Mechanics* **9** 339
- [34] Jawed M K, Khouri N K, Da F, Grinspun E and Reis P M 2015 *Phys. Rev. Lett.* **115** 168101
- [35] Vogel R and Stark H 2012 *Euro. Phys. J. E* **35** 1
- [36] Jawed M K and Reis P M 2016 *Soft Matter* **12** 1898

JUST FOR AUTHORS  
 — CHINESE PHYSICS B

# Chinese Physics B

Volume 31 Number 1 January 2022

## Contents

### TOPICAL REVIEW — Unconventional superconductivity

**017403 Superconductivity in octagraphene**

Jun Li and Dao-Xin Yao

### SPECIAL TOPIC — Superconductivity in vanadium-based kagome materials

**017105 Tri-hexagonal charge order in kagome metal  $\text{CsV}_3\text{Sb}_5$  revealed by  $^{121}\text{Sb}$  nuclear quadrupole resonance**

Chao Mu, Qiangwei Yin, Zhijun Tu, Chunsheng Gong, Ping Zheng, Hechang Lei, Zheng Li and Jianlin Luo

**017106 A density-wave-like transition in the polycrystalline  $\text{V}_3\text{Sb}_2$  sample with bilayer kagome lattice**

Ningning Wang, Yuhao Gu, M. A. McGuire, Jiaqiang Yan, Lifeng Shi, Qi Cui, Keyu Chen, Yuxin Wang, Hua Zhang, Huaixin Yang, Xiaoli Dong, Kun Jiang, Jiangping Hu, Bosen Wang, Jianping Sun and Jinguang Cheng

**017404 Evolution of superconductivity and charge order in pressurized  $\text{RbV}_3\text{Sb}_5$**

Feng Du, Shuaishuai Luo, Rui Li, Brenden R. Ortiz, Ye Chen, Stephen D. Wilson, Yu Song and Huiqiu Yuan

**017405 Pressure tuning of the anomalous Hall effect in the kagome superconductor  $\text{CsV}_3\text{Sb}_5$**

Fang-Hang Yu, Xi-Kai Wen, Zhi-Gang Gui, Tao Wu, Zhenyu Wang, Zi-Ji Xiang, Jianjun Ying and Xianhui Chen

### TOPICAL REVIEW — Non-Hermitian physics

**010307 Efficient and stable wireless power transfer based on the non-Hermitian physics**

Chao Zeng, Zhiwei Guo, Kejia Zhu, Caifu Fan, Guo Li, Jun Jiang, Yunhui Li, Haitao Jiang, Yaping Yang, Yong Sun and Hong Chen

### SPECIAL TOPIC — Non-Hermitian physics

**010308 Non-Hermitian Weyl semimetals: Non-Hermitian skin effect and non-Bloch bulk-boundary correspondence**

Xiaosen Yang, Yang Cao and Yunjia Zhai

**010309 Two-body exceptional points in open dissipative systems**

Peize Ding and Wei Yi

**010310 Topological properties of non-Hermitian Creutz ladders**

Hui-Qiang Liang and Linhu Li

*(Continued on the Bookbinding Inside Back Cover)*

**010311 Disorder in parity–time symmetric quantum walks**

Peng Xue

**010312 Topology of a parity–time symmetric non-Hermitian rhombic lattice**

Shumai Zhang, Liang Jin and Zhi Song

**010313 Exact solutions of non-Hermitian chains with asymmetric long-range hopping under specific boundary conditions**

Cui-Xian Guo and Shu Chen

**014215 Anti- $\mathcal{PT}$ -symmetric Kerr gyroscope**

Huilai Zhang, Meiyu Peng, Xun-Wei Xu and Hui Jing

**017401 Majorana zero modes, unconventional real–complex transition, and mobility edges in a one-dimensional non-Hermitian quasi-periodic lattice**

Shujie Cheng and Xianlong Gao

#### **RAPID COMMUNICATION**

**017502 Probing the magnetization switching with in-plane magnetic anisotropy through field-modified magnetoresistance measurement**

Runrun Hao, Kun Zhang, Yinggang Li, Qiang Cao, Xueying Zhang, Dapeng Zhu and Weisheng Zhao

**018202 Substrate tuned reconstructed polymerization of naphthalocyanine on Ag(110)**

Qi Zheng, Li Huang, Deliang Bao, Rongting Wu, Yan Li, Xiao Lin, Shixuan Du and Hong-Jun Gao

#### **GENERAL**

**010201 Soliton molecules and asymmetric solitons of the extended Lax equation via velocity resonance**

Hongcai Ma, Yuxin Wang and Aiping Deng

**010202 Theoretical study of (e, 2e) triple differential cross sections of pyrimidine and tetrahydrofurfuryl alcohol molecules using multi-center distorted-wave method**

Yiao Wang, Zhenpeng Wang, Maomao Gong, Chunkai Xu and Xiangjun Chen

**010301 Protection of entanglement between two V-atoms in a multi-cavity coupling system**

Wen-Jin Huang, Mao-Fa Fang and Xiong Xu

**010302 Semi-quantum private comparison protocol of size relation with  $d$ -dimensional GHZ states**

Bing Wang, San-Qiu Liu and Li-Hua Gong

**010303 Determination of quantum toric error correction code threshold using convolutional neural network decoders**

Hao-Wen Wang, Yun-Jia Xue, Yu-Lin Ma, Nan Hua and Hong-Yang Ma

**010304 Low-loss belief propagation decoder with Tanner graph in quantum error-correction codes**

Dan-Dan Yan, Xing-Kui Fan, Zhen-Yu Chen and Hong-Yang Ma

**010305 Quantum multicast communication over the butterfly network**

Xing-Bo Pan, Xiu-Bo Chen, Gang Xu, Zhao Dou, Zong-Peng Li and Yi-Xian Yang

- 010306 Vacuum-gap-based lumped element Josephson parametric amplifier**  
Sishi Wu, Dengke Zhang, Rui Wang, Yulong Liu, Shuai-Peng Wang, Qichun Liu, J S Tsai and Tiefu Li
- 010314 Dynamical learning of non-Markovian quantum dynamics**  
Jintao Yang, Junpeng Cao and Wen-Li Yang
- 010501 Nonlinear dynamics analysis of cluster-shaped conservative flows generated from a generalized thermostatted system**  
Yue Li, Zengqiang Chen, Zenghui Wang and Shijian Cang
- 010502 A new simplified ordered upwind method for calculating quasi-potential**  
Qing Yu and Xianbin Liu
- 010503 Explosive synchronization in a mobile network in the presence of a positive feedback mechanism**  
Dong-Jie Qian
- 010504 An extended smart driver model considering electronic throttle angle changes with memory**  
Congzhi Wu, Hongxia Ge and Rongjun Cheng
- 010505 Large-amplitude dust acoustic solitons in an opposite polarity dusty plasma with generalized polarization force**  
Mahmood A. H. Khaled, Mohamed A. Shukri and Yusra A. A. Hager
- 010701 Effect of staggered array structure on the flow field of micro gas chromatographic column**  
Daohan Ge, Zhou Hu, Liqiang Zhang and Shining Zhu
- 010702 Instantaneous frequency measurement using two parallel I/Q modulators based on optical power monitoring**  
Chuangye Wang, Tigang Ning, Jing Li, Li Pei, Jingjing Zheng and Jingchuan Zhang

#### ATOMIC AND MOLECULAR PHYSICS

- 013101 M1 transition energy and rate in the ground configuration of Ag-like ions with  $62 \leq Z \leq 94$**   
Ju Meng, Wen-Xian Li, Ji-Guang Li, Ze-Qing Wu, Jun Yan, Yong Wu and Jian-Guo Wang
- 013201 Solving the time-dependent Schrödinger equation by combining smooth exterior complex scaling and Arnoldi propagator**  
Shun Wang and Wei-Chao Jiang
- 013202 Influence of Coulomb force between two electrons on double ionization of He-like atoms**  
Peipei Liu, Yongfang Li and Jingtao Zhang
- 013401 Electron-impact ionization cross section calculations for lithium-like ions**  
Guo-Jie Bian, Jyh-Ching Chang, Ke-Ning Huang, Chen-Sheng Wu, Yong-Jun Cheng, Kai Wang and Yong Wu

**ELECTROMAGNETISM, OPTICS, ACOUSTICS, HEAT TRANSFER, CLASSICAL MECHANICS, AND FLUID DYNAMICS**

- 014101 Tunable terahertz transmission behaviors and coupling mechanism in hybrid MoS<sub>2</sub> meta-materials**  
Yuwang Deng, Qingli Zhou, Wanlin Liang, Pujing Zhang and Cunlin Zhang
- 014102 High-confinement ultra-wideband bandpass filter using compact folded slotline spoof surface plasmon polaritons**  
Xue-Wei Zhang, Shao-Bin Liu, Ling-Ling Wang, Qi-Ming Yu, Jian-Lou and Shi-Ning Sun
- 014201 Bandwidth-tunable silicon nitride microring resonators**  
Jiacheng Liu, Chao Wu, Gongyu Xia, Qilin Zheng, Zhihong Zhu and Ping Xu
- 014202 High-efficiency asymmetric diffraction based on PT-antisymmetry in quantum dot molecules**  
Guangling Cheng, Yongsheng Hu, Wenxue Zhong and Aixi Chen
- 014203 Propagation dynamics of dipole breathing wave in lossy nonlocal nonlinear media**  
Jian-Li Guo, Zhen-Jun Yang, Xing-Liang Li and Shu-Min Zhang
- 014204 High-energy picosecond single-pass multi-stage optical parametric generator and amplifier**  
Yang Yu, Zhao Liu, Ke Liu, Chao Ma, Hong-Wei Gao, Xiao-Jun Wang, Yong Bo, Da-Fu Cui and Qin-Jun Peng
- 014205 Photonic spin Hall effect and terahertz gas sensor via InSb-supported long-range surface plasmon resonance**  
Jie Cheng, Gaojun Wang, Peng Dong, Dapeng Liu, Fengfeng Chi and Shengli Liu
- 014206 Plasmonic sensor with self-reference capability based on functional layer film composed of Au/Si gratings**  
Jiankai Zhu, Xiangxian Wang, Yunping Qi and Jianli Yu
- 014207 Wavelength and sensitivity tunable long period gratings fabricated in fluid-cladding microfibers**  
Wa Jin, Linke Zhang, Xiang Zhang, Ming Xu, Weihong Bi and Yuefeng Qi
- 014208 Topological phases and type-II edge state in two-leg-coupled Su-Schrieffer-Heeger chains**  
Tianqi Luo, Xin Guan, Jingtao Fan, Gang Chen and Suo-Tang Jia
- 014209 Brightening single-photon emitters by combining an ultrathin metallic antenna and a silicon quasi-BIC antenna**  
Shangtong Jia, Zhi Li and Jianjun Chen
- 014210 Hidden symmetry operators for asymmetric generalized quantum Rabi models**  
Xilin Lu, Zi-Min Li, Vladimir V Mangazeev and Murray T Batchelor
- 014211 Wideband switchable dual-functional terahertz polarization converter based on vanadium dioxide-assisted metasurface**  
De-Xian Yan, Qin-Yin Feng, Zi-Wei Yuan, Miao Meng, Xiang-Jun Li, Guo-Hua Qiu and Ji-Ning Li

- 014212 Research of NO<sub>2</sub> vertical profiles with look-up table method based on MAX-DOAS**  
Yingying Guo, Suwen Li, Fusheng Mou, Hexiang Qi and Qijin Zhang
- 014213 A 515-nm laser-pumped idler-resonant femtosecond BiB<sub>3</sub>O<sub>6</sub> optical parametric oscillator**  
Jinfang Yang, Zhaohua Wang, Jiajun Song, Renchong Lv, Xianzhi Wang, Jiangfeng Zhu and Zhiyi Wei
- 014214 Lattice plasmon mode excitation via near-field coupling**  
Yun Lin, Shuo Shen, Xiang Gao and Liancheng Wang
- 014216 Mode splitting and multiple-wavelength managements of surface plasmon polaritons in coupled cavities**  
Ping-Bo Fu and Yue-Gang Chen
- 014217 Quality factor enhancement of plasmonic surface lattice resonance by using asymmetric periods**  
Yunjie Shi, Lei Xiong, Yuming Dong, Degui Sun and Guangyuan Li
- 014301 Microcrack localization using a collinear Lamb wave frequency-mixing technique in a thin plate**  
Ji-Shuo Wang, Cai-Bin Xu, You-Xuan Zhao, Ning Hu and Ming-Xi Deng
- 014401 Thermal apoptosis analysis considering injection behavior optimization and mass diffusion during magnetic hyperthermia**  
Yun-Dong Tang, Jian Zou, Rodolfo C C Flesch, Tao Jin and Ming-Hua He
- 014402 Construction and mechanism analysis on nanoscale thermal cloak by *in-situ* annealing silicon carbide film**  
Jian Zhang, Hao-Chun Zhang, Zi-Liang Huang, Wen-Bo Sun and Yi-Yi Li
- 014501 Three-dimensional clogging structures of granular spheres near hopper orifice**  
Jing Yang, Dianjinfeng Gong, Xiaoxue Wang, Zhichao Wang, Jianqi Li, Bingwen Hu and Chengjie Xia
- 014701 Characteristics of temperature fluctuation in two-dimensional turbulent Rayleigh–Bénard convection**  
Ming-Wei Fang, Jian-Chao He, Zhan-Chao Hu and Yun Bao
- 014702 Speedup of self-propelled helical swimmers in a long cylindrical pipe**  
Ji Zhang, Kai Liu and Yang Ding
- 014703 *In situ* measurement on nonuniform velocity distribution in external detonation exhaust flow by analysis of spectrum features using TDLAS**  
Xiao-Long Huang, Ning Li, Chun-Sheng Weng and Yang Kang
- CONDENSED MATTER: STRUCTURAL, MECHANICAL, AND THERMAL PROPERTIES**
- 016101 Mechanism of microweld formation and breakage during Cu–Cu wire bonding investigated by molecular dynamics simulation**  
Beikang Gu, Shengnan Shen and Hui Li

**016102 First-principles study of structural and opto-electronic characteristics of ultra-thin amorphous carbon films**

Xiao-Yan Liu, Lei Wang and Yi Tong

**016103 Polymorph selection of magnesium under different pressures: A simulation study**

Wei Liu, Boqiang Wu, Ze'an Tian, Yunfei Mo, Tingfei Xi, Zhiyi Wan, Rangsu Liu and Hairong Liu

**016104 Pressure dependence of the thermal stability in  $\text{LiMn}_2\text{O}_4$**

Yan Zeng, Hao Liang, Shixue Guan, Junpu Wang, Wenjia Liang, Mengyang Huang and Fang Peng

**016105 Spin and spin-orbit coupling effects in nickel-based superalloys: A first-principles study on  $\text{Ni}_3\text{Al}$  doped with Ta/W/Re**

Liping Liu, Jin Cao, Wei Guo and Chongyu Wang

**016106 Probing structural and electronic properties of divalent metal  $\text{Mg}_{n+1}$  and  $\text{SrMg}_n$  ( $n = 2-12$ ) clusters and their anions**

Song-Guo Xi, Qing-Yang Li, Yan-Fei Hu, Yu-Quan Yuan, Ya-Ru Zhao, Jun-Jie Yuan, Meng-Chun Li and Yu-Jie Yang

**016401 Role of compositional changes on thermal, magnetic, and mechanical properties of Fe-P-C-based amorphous alloys**

Indah Raya, Supat Chupradit, Mustafa M Kadhim, Mustafa Z Mahmoud, Abduladheem Turki Jalil, Aravindhan Surendar, Sukaina Tuama Ghafel, Yasser Fakri Mustafa and Alexander N Bocharov

**016701 Observation of the BEC-BCS crossover in a degenerate Fermi gas of lithium atoms**

Xiang-Chuan Yan, Da-Li Sun, Lu Wang, Jing Min, Shi-Guo Peng and Kai-Jun Jiang

**016702 Observation of photon recoil effects in single-beam absorption spectroscopy with an ultracold strontium gas**

Fachao Hu, Canzhu Tan, Yuhai Jiang, Matthias Weidemüller and Bing Zhu

**016801 Three-dimensional vertical ZnO transistors with suspended top electrodes fabricated by focused ion beam technology**

Chi Sun, Linyuan Zhao, Tingting Hao, Renrong Liang, Haitao Ye, Junjie Li and Changzhi Gu

**CONDENSED MATTER: ELECTRONIC STRUCTURE, ELECTRICAL, MAGNETIC, AND OPTICAL PROPERTIES**

**017101 Pressure- and temperature-dependent luminescence from  $\text{Tm}^{3+}$  ions doped in  $\text{GdYTaO}_4$**

Peng-Yu Zhou, Xiu-Ming Dou, Bao-Quan Sun, Ren-Qin Dou, Qing-Li Zhang, Bao Liu, Pu-Geng Hou, Kai-Lin Chi and Kun Ding

**017102  $SU(3)$  spin-orbit coupled fermions in an optical lattice**

Xiaofan Zhou, Gang Chen and Suo-Tang Jia

**017103 Defect calculations with quasiparticle correction: A revisited study of iodine defects in  $\text{CH}_3\text{NH}_3\text{PbI}_3$**

Ling Li and Wan-Jian Yin

- 017104 First-principles study on improvement of two-dimensional hole gas concentration and confinement in AlN/GaN superlattices**  
Huihui He and Shenyuan Yang
- 017201 Separating spins by dwell time of electrons across parallel double  $\delta$ -magnetic-barrier nanostructure applied by bias**  
Sai-Yan Chen, Mao-Wang Lu and Xue-Li Cao
- 017301 Dependence of short channel length on negative/positive bias temperature instability (NBTI/PBTI) for 3D FinFET devices**  
Ren-Ren Xu, Qing-Zhu Zhang, Long-Da Zhou, Hong Yang, Tian-Yang Gai, Hua-Xiang Yin and Wen-Wu Wang
- 017302 Spin transport properties for B-doped zigzag silicene nanoribbons with different edge hydrogenations**  
Jing-Fen Zhao, Hui Wang, Zai-Fa Yang, Hui Gao, Hong-Xia Bu and Xiao-Juan Yuan
- 017303 Light focusing in linear arranged symmetric nanoparticle trimer on metal film system**  
Yuxia Tang, Shuxia Wang, Yingzhou Huang and Yurui Fang
- 017304 Study on a novel vertical enhancement-mode Ga<sub>2</sub>O<sub>3</sub> MOSFET with FINFET structure**  
Liangliang Guo, Yuming Zhang, Suzhen Luan, Rundi Qiao and Renxu Jia
- 017305 Integer quantum Hall effect in Kekulé-patterned graphene**  
Yawar Mohammadi and Samira Bahrami
- 017402 Cross correlation mediated by distant Majorana zero modes with no overlap**  
Lupei Qin, Wei Feng and Xin-Qi Li
- 017501 Perpendicular magnetic anisotropy of Pd/Co<sub>2</sub>MnSi/NiFe<sub>2</sub>O<sub>4</sub>/Pd multilayers on F-mica substrates**  
Qingwang Bai, Bin Guo, Qin Yin and Shuyun Wang
- 017601 Theoretical investigation of ferromagnetic resonance in a ferromagnetic thin film with external stress anisotropy**  
Jieyu Zhou, Jianhong Rong, Huan Wang, Guohong Yun, Yanan Wang and Shufei Zhang
- 017701 Observation of source/drain bias-controlled quantum transport spectrum in junctionless silicon nanowire transistor**  
Yang-Yan Guo, Wei-Hua Han, Xiao-Di Zhang, Jun-Dong Chen and Fu-Hua Yang
- 017801 Efficiency droop in InGaN/GaN-based LEDs with a gradually varying In composition in each InGaN well layer**  
Shang-Da Qu, Ming-Sheng Xu, Cheng-Xin Wang, Kai-Ju Shi, Rui Li, Ye-Hui Wei, Xian-Gang Xu and Zi-Wu Ji
- 017802 Magnetic polaron-related optical properties in Ni(II)-doped CdS nanobelts: Implication for spin nanophotonic devices**  
Fu-Jian Ge, Hui Peng, Ye Tian, Xiao-Yue Fan, Shuai Zhang, Xian-Xin Wu, Xin-Feng Liu and Bing-Suo Zou

**017803 Uniform light emission from electrically driven plasmonic grating using multilayer tunneling barriers**

Xiao-Bo He, Hua-Tian Hu, Ji-Bo Tang, Guo-Zhen Zhang, Xue Chen, Jun-Jun Shi, Zhen-Wei Ou, Zhi-Feng Shi, Shun-Ping Zhang, Chang Liu and Hong-Xing Xu

**017804 Demonstration of Faraday anomalous dispersion optical filter with reflection configuration**

Yi Liu, Baodong Yang, Junmin Wang, Wenyi Huang, Zhiyu Gou and Haitao Zhou

**017901 Two different emission enhancement of trans-stilbene crystal under high pressure: Different evolution of structure**

Yarong Gu, Guicheng Shao, Zhumei Tian, Haixia Li, Kai Wang and Bo Zou

#### INTERDISCIPLINARY PHYSICS AND RELATED AREAS OF SCIENCE AND TECHNOLOGY

**018101 Removal of GaN film over AlGaIn with inductively coupled BCl<sub>3</sub>/Ar atomic layer etch**

Jia-Le Tang and Chao Liu

**018102 Plasma assisted molecular beam epitaxial growth of GaN with low growth rates and their properties**

Zhen-Hua Li, Peng-Fei Shao, Gen-Jun Shi, Yao-Zheng Wu, Zheng-Peng Wang, Si-Qi Li, Dong-Qi Zhang, Tao Tao, Qing-Jun Xu, Zi-Li Xie, Jian-Dong Ye, Dun-Jun Chen, Bin Liu, Ke Wang, You-Dou Zheng and Rong Zhang

**018103 Synthesis and study the influence of yttrium doping on band structure, optical, non-linear optical and dielectric results for Ca<sub>12</sub>Al<sub>14</sub>O<sub>33</sub> (C12A7) single crystals grown using traveling-solvent floating zone (TSFZ) method**

A. Abdel Moez, Ahmed I. Ali and A. Tayel

**018201 Theoretical study on the exciton dynamics of coherent excitation energy transfer in the phycoerythrin 545 light-harvesting complex**

Xue-Yan Cui, Yi-Jing Yan and Jian-Hua Wei

**018401 Modeling and character analyzing of multiple fractional-order memcapacitors in parallel connection**

Xiang Xu, Gangquan Si, Zhang Guo and Babajide Oluwatosin Oresanya

**018501 Sensitivity of heavy-ion-induced single event burnout in SiC MOSFET**

Hong Zhang, Hong-Xia Guo, Feng-Qi Zhang, Xiao-Yu Pan, Yi-Tian Liu, Zhao-Qiao Gu, An-An Ju and Xiao-Ping Ouyang

**018502 Heterogeneous integration of InP HEMTs on quartz wafer using BCB bonding technology**

Yan-Fu Wang, Bo Wang, Rui-Ze Feng, Zhi-Hang Tong, Tong Liu, Peng Ding, Yong-Bo Su, Jing-Tao Zhou, Feng Yang, Wu-Chang Ding and Zhi Jin

**018503 Voltage-controllable magnetic skyrmion dynamics for spiking neuron device applications**

Ming-Min Zhu, Shu-Ting Cui, Xiao-Fei Xu, Sheng-Bin Shi, Di-Qing Nian, Jing Luo, Yang Qiu, Han Yang, Guo-Liang Yu and Hao-Miao Zhou

- 018504 A 3D SiC MOSFET with poly-silicon/SiC heterojunction diode**  
Sheng-Long Ran, Zhi-Yong Huang, Sheng-Dong Hu, Han Yang, Jie Jiang and Du Zhou
- 018505 Impact of symmetric gate-recess length on the DC and RF characteristics of InP HEMTs**  
Ruize Feng, Bo Wang, Shurui Cao, Tong Liu, Yongbo Su, Wuchang Ding, Peng Ding and Zhi Jin
- 018506 A novel low-loss four-bit bandpass filter using RF MEMS switches**  
Lulu Han, Yu Wang, Qiannan Wu, Shiyi Zhang, Shanshan Wang and Mengwei Li
- 018701 Social bots and mass media manipulated public opinion through dual opinion climate**  
Chun Cheng, Yun Luo, Chang-bin Yu and Wei-ping Ding
- 018801 High efficiency ETM-free perovskite cell composed of CuSCN and increasing gradient  $\text{CH}_3\text{NH}_3\text{PbI}_3$**   
Tao Wang, Gui-Jiang Xiao, Ren Sun, Lin-Bao Luo and Mao-Xiang Yi
- 018901 Cascading failures of overload behaviors using a new coupled network model between edges**  
Yu-Wei Yan, Yuan Jiang, Rong-Bin Yu, Song-Qing Yang and Cheng Hon
- 018902 Information flow between stock markets: A Koopman decomposition approach**  
Semba Sherehe, Huiyun Wan, Changgui Gu and Huijie Yang

JUST FOR AUTHORS  
— CHINESE PHYSICS B